Time-Series Analysis and Prediction of Surface Deformation in the Jinchuan Mining Area, Gansu Province, by Using InSAR and CNN–PhLSTM Network

Yi He ⬥, Haowen Yan, Wang Yang ⬥, Sheng Yao ⬥, Lifeng Zhang, Yi Chen ⬥, and Tao Liu

Abstract—Surface deformation poses a great threat to the safety of Jinchuan mining area production activities. At present, the spatio-temporal evolution law and mechanism of surface deformation in the Jinchuan mining area are unclear, and it is difficult to obtain reliable prediction results using the existing spatio-temporal prediction methods due to the lack of model parameters or relevant data. To solve these problems, this study proposes a new unified convolutional neural network with peephole long short-term memory (CNN-PhLSTM). Small baseline subset interferometric synthetic aperture radar (SBAS-InSAR) technology was used to obtain the spatio-temporal evolution characteristics of surface deformation in the period of 2014–2021. Time series InSAR deformation data are merged into a unified network model in series with a time-distributed CNN segmentation and stacked PhLSTM. The InSAR measurement results are shown to be reliable by comparison and verification with the benchmark and InSAR results of different orbits. The proposed CNN-PhLSTM model was evaluated by mean absolute error and structural similarity (SSIM) evaluation indexes, and was compared with support vector regression (SVR), multilayer perceptron (MLP) and CNN-LSTM models. The results show three continuous subsidence areas, namely the Longshou, second western and third eastern mining areas. The cumulative surface deformation continued to increase from 2014 to 2021. Faults and lithology control the spatial distribution of surface deformation in the Jinchuan mining area. The prediction results demonstrate that the surface deformation range will continue to expand and that time-series surface deformation will show a slow deceleration trend in the next two years.

I. INTRODUCTION

MINERAL resources have played a significant role in promoting China's economic development, with the mining economy accounting for 5.5% of China's GDP. However, the large-scale exploitation of mineral resources inevitably leads to surface deformation, surface collapse, and other potential disasters [1]. According to the survey results of the China Institute of Geological Environment Monitoring, at the end of 2015, the volume of mined-out sites formed by underground mining in China reached 12.8×10^6 m^3, causing a variety of geological disasters, such as mine collapse and collapse, resulting in a large number of property losses, and casualties [2]. A typical example of this phenomenon is the surface subsidence of a mined-out area in the Zhaoyuan gold mine in Shandong Province, which led to the destruction of a large area of highway and major economic losses, according to the results of a national mine geological environment survey. In the face of such a serious surface deformation problem, it is necessary to monitor and predict the spatiotemporal characteristics of surface deformation in mining areas in real time [3], [4].

Many scholars have used global position system (GPS) and leveling methods for the real-time monitoring of surface deformation in mining areas [5], [6], [7], but these methods have the disadvantages of small monitoring range, low monitoring efficiency, high cost, and low monitoring site density [8]. Interferometric synthetic aperture radar (InSAR) is a high-precision measurement technology that uses phase differences to obtain information about surface deformation [9], [10], [11]. Compared with traditional methods, InSAR has a higher density of monitoring points, a larger monitoring range, and a higher monitoring efficiency [12], [13]. The research results of many scholars prove that InSAR technology is an effective method for monitoring surface deformation in mining areas [14], [15], [16], [17], [18]. For example, Li et al. [19] evaluated the stability of residential buildings in the Huaian mining area by combining a time-series InSAR analysis method with an empirical model of building damage levels. Ma et al. [20] investigated

and analyzed mining deformation in the Shendong coal field using small baseline subset InSAR (SBAS-InSAR) technology. Yang et al. [21] estimated the model parameters of the probability integral method based on the line-of-sight (LOS) deformation derived from the InSAR. The selection of radar data is also crucial for monitoring surface deformation to ensure the accuracy of the monitoring in mining areas. Currently available sources of radar data include Sentinel-1A (C band), ALOS (L band), TerraSAR-X (X band), COSMO-SkyMed (X band), Gaofen-3 (C band), and TanDEM-X (X band). Sentinel-1A has been widely used in monitoring surface deformation in mining areas due to its free usage, large data coverage, short return cycle, and high data quality [22], [23].

For the predictive simulation of surface deformation's temporal sequence, some scholars used empirical models [24], mathematical statistical models [25], [26], and machine learning models [27]. Empirical models have a series of complex parameters, and most cases require assumptions to be made, so it is difficult to establish a good prediction model [28]. Mathematical statistical models usually require a large amount of historical monitoring data, which is time-consuming and laborious to obtain, and has a high cost, so it is difficult to use such models widely [29]. Machine learning models are not affected by complex geological and hydrological physical parameters. They also widely used the regression of ideas, which is closely related to temporal prediction [30], mainly in the form models, such as the support vector machines [31], long short-term memory (LSTM) [27] and heterogeneous LSTM neural networks [32]. However, these machine learning models are based on time-series forecasting data, so the nonlinear fitting of the deformation time series is realized by piecewise linear approximation, which essentially ignores the nonlinear correlation in the time series and cannot predict a spatial trend based on the raster image data. Therefore, there is an urgent need to establish an effective prediction model for surface deformation using InSAR raster image data. Convolutional neural networks (CNNs) can actively learn image features and are good at extracting spatial information [30]. Peephole long short-term memory (PhLSTM) has sequence memory, and is good at processing sequence input and can learn the fine distinctions between sequences of spikes spaced without the help of any short training exemplars [33]. This article studies a unified network of information made up of a CNN and PhLSTM that considers spatial and time series to improve the prediction accuracy.

The Jinchuan mining area is China's largest nickel ore mining base, and the Longshou mining area as one of the main mining areas of the Jinchuan nickel mine [34]. Due to years of mining in this area, in 2016, mining was stopped in the closed circular crack. The bottomless pillar sublevel caving method was adopted for the first time in 2019 to enable mining to continue, as this method provides mining strength with a high degree of mechanization and relatively low mining cost. However, the bottomless pillar subcaving method results in a high level of surface deformation [35]. Surface deformation is the impactful secondary disaster in the Jinchuan mining area and poses a great threat to the safety of production activities in the mining area [36]. Therefore, it is necessary to monitor the surface deformation

resulting from mining by the pillarless sublevel caving method in the Jinchuan mining area. Ding et al. [37] used SBAS-InSAR technology to study the deformation of the Longshou open-pit in the Jinchuan mining area from 2009 to 2016, and analyzed its 3-D characteristics. Li [36] combined SBAS-InSAR, unmanned aerial photogrammetry tilt, and leveling technology to study the law of surface deformation in the industrial pilot area of the Longshou mining area in Jinchuan. Sun et al. [38] studied the deformation and failure mechanisms of the vertical shaft in the Jinchuan No. 2 mining area. The above research has guiding significance for further study of surface deformation in the Jinchuan mining area, but no detailed analysis of the spatiotemporal characteristics of the Jinchuan mine has been conducted, and no predictive simulation of its spatiotemporal evolution trend has been reported.

The specific objectives of the present article are as follows: 1) to obtain the spatiotemporal evolution characteristics of surface deformation in the Jinchuan mining area from 2014 to 2021 based on Sentinel-1A data using SBAS-InSAR technology; 2) to propose a CNN–PhLSTM deep neural network model to simulate and predict spatiotemporal surface deformation using time-series InSAR deformation data; and 3) to analyze the future spatiotemporal evolution trend of surface deformation.

II. STUDY AREA AND DATA SOURCE

A. Study Area

The Jinchuan mining area in Jinchang City, Gansu Province, is located in the southwest margin of the Alxa platform, to the north of the Lonshoushan fold belt. In the south, this mining area is adjacent to the corridor transition zone north of the Qiliangari fold belt (Fig. 1). This region has China's largest nickel deposits and is the country's main producer of platinum. The lithology of the Jinchuan mining area changes frequently, and the rock mass is dominated by an ore-bearing ultra-basic rock mass. The ore body is composed of nickel sulphide rich ore and copper sulphide ore, among which the nickel sulphide rich ore can be divided into penetration type, ultra-basic type, and contact metasomatic type rock [35]. The Jinchuan mining area is characterized by a weak structure, and the stability of rock mass in the mining area is very poor due to faults of different sizes and different types of contact zones [36], [39]. These characteristics have increased with the strength of mining activities in recent years, the deepening level of mining, and *in-situ* stress structural conditions of the mining complex. The head of the mining surface subsidence is always a significant threat to the safety of the Longshou mining area's production. Therefore, real-time monitoring of surface deformation and spatiotemporal prediction of surface deformation are important to ensure the safety of this mining area [37].

B. Data

This article adopted the cover study area from October 14, 2014 to April 16, 2021, using 156 IW mode track no.128 ascending Sentinel-1A data (https://search.asf.alaska.edu/), the incidence angle θ was 34.17°, and the azimuth was 186.94°. In
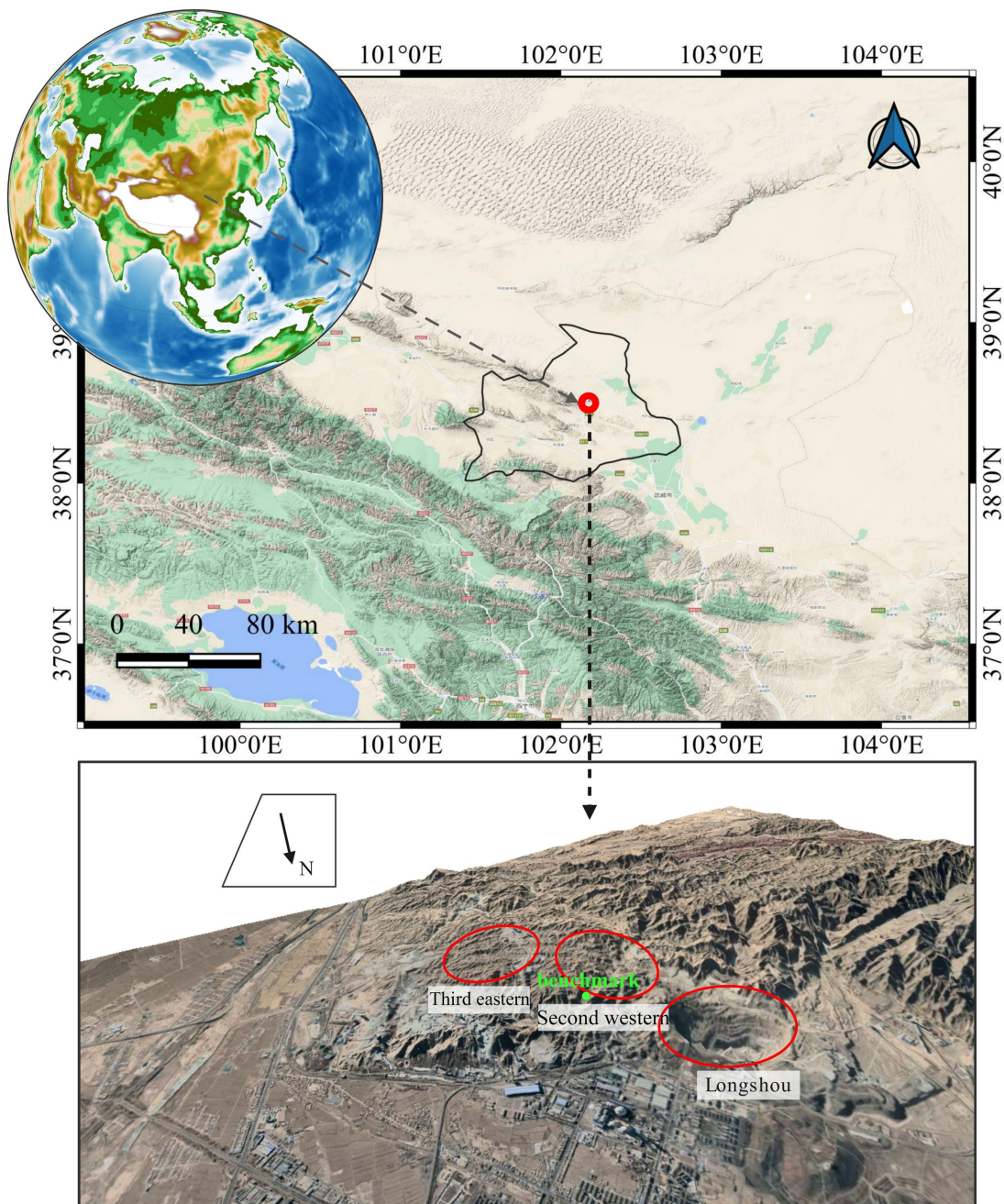
Fig. 1.   Geographical location of the study area.

addition, 71 orbital descending images of track no.135 (March 27, 2018–October 11, 2020) were selected for cross-validation of InSAR results, the incidence angle θ was 41.42°, and the azimuth was 354.70°. SBAS–InSAR technology was used to monitor the deformation rate and cumulative time-series deformation in the study area. Digital elevation model (DEM) data from Shuttle Radar Probe Mission 90-m spatial resolution were used for orbit refining and flattening (http://www.gscloud.cn/). To verify the validity and accuracy of the InSAR deformation monitoring results in this article, a benchmark data was selected to test the InSAR time-series results in the study area [38].

Faults and lithology were analyzed to determine the deformation mechanism.

III. METHODOLOGY

In this article, SBAS–InSAR technology was first used to monitor the spatiotemporal deformation of the Jinchuan mining area from 2014 to 2021, based on Sentinel-1A orbit lifting data. A CNN–PhLSTM deep neural network method was constructed to predict the future temporal and spatial evolution trends of surface deformation. The specific research framework is shown
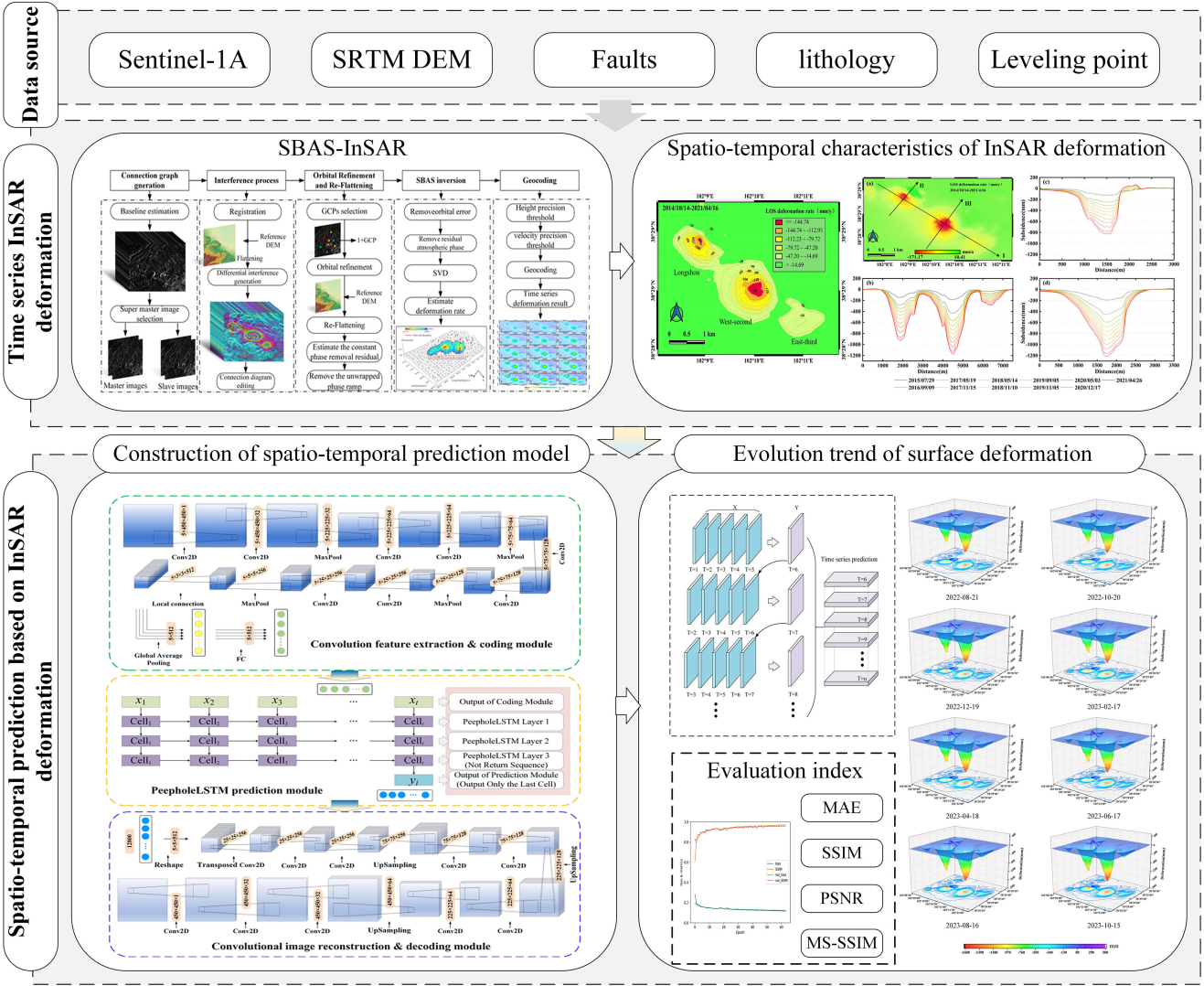
Fig. 2. Overall research framework.

in Fig. 2, and the detailed process for each part of the proposed method is shown.

A. SBAS–InSAR Method

An SBAS–InSAR is an improved time-series analysis technology proposed by Berardino in 2002 [40]. SBAS–InSAR technology generates time-series interferences based on different images by combining image pairs within a certain time baseline and space baseline. The space and time baselines of Synthetic Aperture Radar (SAR) images within the sets are small, but the space and time baselines between the sets are large, which can minimize potential errors and incoherence caused by perspective differences. Then, conventional differential interference processing was performed for the interference pairs in the sets, using the singular value decomposition (SVD) method. Each deformation of the phase transition is linked to the deformation phase of a particular image. Then, temporal low-pass filtering

and spatial domain high-pass filtering are used to remove the influence of the atmosphere, and the resulting deformation of the final result will be obtained.

Additional short baseline sets are applied to combine the technology, alleviate the impact of atmospheric delay, and improve the monitoring time resolution. The time discontinuity problem caused by too-long spatial baselines between various datasets can be effectively solved, and the time-series results and deformation rate of the entire observation period can be obtained [13]. The processing of data on surface deformation acquired by SBAS–InSAR technology includes seven main steps: data preprocessing, connection graph generation, differential interferogram generation, orbit refining and reflattening, SBAS inversion, geocoding and LOS deformation visualization. The specific process is shown in Fig. 3.

The processing flow of SBAS–InSAR technology applied SARscape5.6 on environment for visualizing images (ENVI) platform is described in detail as follows:
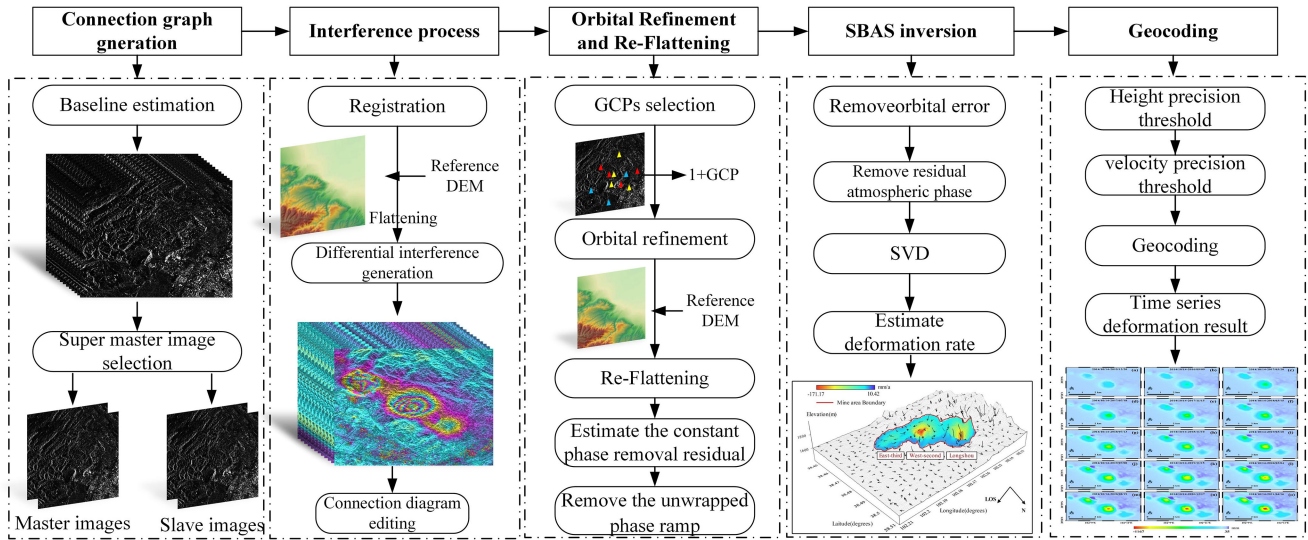
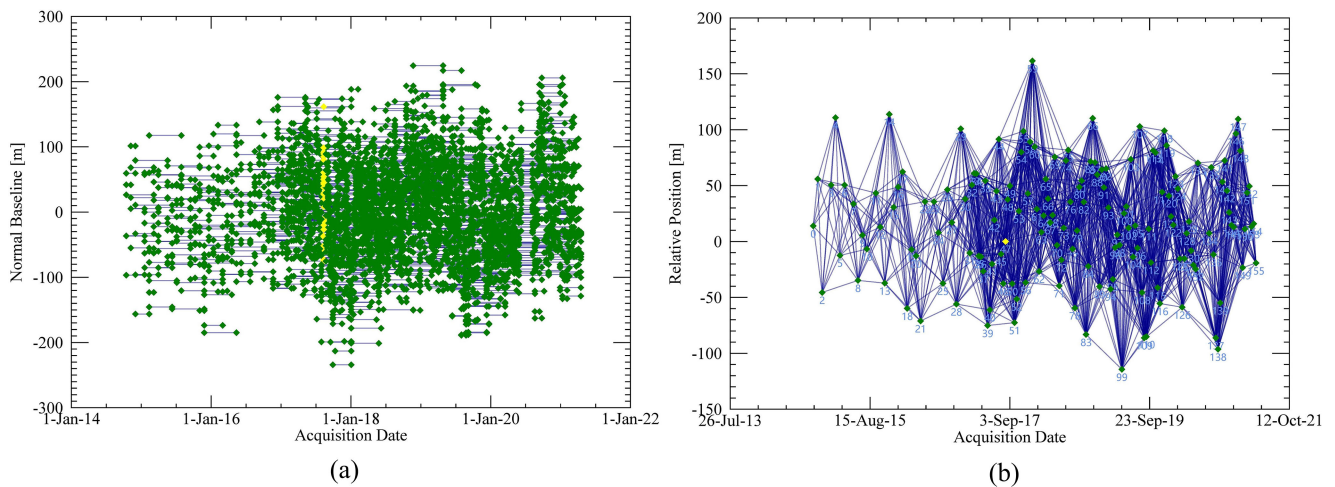Fig. 3.   Data processing flow of SBAS–InSAR technology.

Fig. 4.   Spatiotemporal baseline diagram.

1) *Data preprocessing:* 156 Sentinel-1A images were imported into ENVI and clipped images according to the study area.

2) *Connection graph generation:* The time baseline was 200 days, the spatial baseline was set at 20% of the critical baseline, and the image taken on September 3, 2017, with the optimal Doppler centroid frequency was selected as the super primary image (Fig. 4).

3) *Differential interferogram generation:* All secondary images were registered and sampled to the super primary image, and then M image pairs were interfered to obtain M interferogram. In order to increase the signal-to-noise ratio of the interferogram, provide more reliable coherence, and improve the calculation efficiency of large-scale data range, multiview processing was performed for each interferogram in the range direction and azimuth direction. The topographic phase was simulated by using external

reference DEM data and was differentiated with the interferogram to obtain the differential interferogram which removed topographic phase. The unwrapping method used was Delaunay minimum cost flow. The baseline tool was used to screen the interferograms and remove any of poor quality.

4) *Orbit refining and reflattening:* A certain number of highly coherent control points were selected in the study area. The residual phase in the initial unwrapping phase was estimated according to these control points' phase information and removed the residual terrain phase.

5) *SBAS inversion:* In the first inversion, a linear model was used to estimate the deformation rate and residual terrain, and the input interferogram was optimized using quadratic unwinding. The SVD method was used to obtain time-series surface deformation. In the second inversion, low- and high-pass filters were used to remove the atmospheric

phase, and the final deformation rate and shape variables were obtained.

6) *Geocoding:* The coherence coefficient of SBAS–InSAR inversion is 0.85, and the result of SBAS–InSAR inversion is converted to the geographic coordinate system.

7) *Result visualization:* After geocoding, the vector files are mapped and outputted by QGIS software.

B. Spatiotemporal Prediction Method for InSAR Deformation Data

1) Preprocessing of InSAR Deformation Data

a) Compression method of InSAR deformation data: The spatiotemporal InSAR deformation data from the Jinchuan mining area, based on SBAS–InSAR technology, have great differences in overall data, training, and prediction. Using traditional compression methods leads to gradient disappearance and affecting prediction accuracy. Alternatively, gate recurrent units (GRUs) effectively address sequence problems and avoid gradient disappearance and explosion [41]. The network is composed of two gate functions: the update and the reset gates [42]. The update gate accumulates conditional leakage and can linearly control any dimension to copy or update it. The reset gate controls the current state for the next state and introduces additional nonlinear effects between sequences [30]. For these reasons, a GRU was used to compress InSAR deformation data.

Numerical compression processing is carried out from the minimum and maximum perspectives from InSAR deformation data. Sequence information is formed for the minimum and maximum by penetrating the spatiotemporal InSAR deformation data sequence grid extremum. The minimum and maximum fitting sequences must be normalized, and a GRU is constructed to train and predict data. The minimum and maximum sequences are input into two identical GRU submodels, each of which is composed of three GRU layers. Finally, the concatenate function combines the predicted results so that the GRU submodels can complete the training and prediction process together. The minimum and maximum spatiotemporal predictions for the mining area were obtained. The loss function is a logarithmic hyperbolic cosine function (LogCosh), the evaluation metric is cosine similarity, time step is 15, epoch is 64, train batch size is 64, and learning rate is 1×10^{-5}. The curves of the loss function and evaluation metrics in the training and validation set during the training process are shown in Fig. 5.

LogCosh is another loss function applied to regression tasks and is smoother than mean square error loss functions. LogCosh is the logarithm of the hyperbolic cosine for the prediction error. The LogCosh equation is as follows:

$$\text{LogCosh}\left(y, y^p\right) = \sum_i^n \log\left(\cosh\left(y_i^p - y_i\right)\right). \tag{1}$$

Cosine similarity measures the difference between two individuals using the cosine of the angle between two vectors in the vector space. Compared to the distance measure, cosine similarity pays attention to the difference between two vectors in direction rather than distance or length. Cosine similarity is
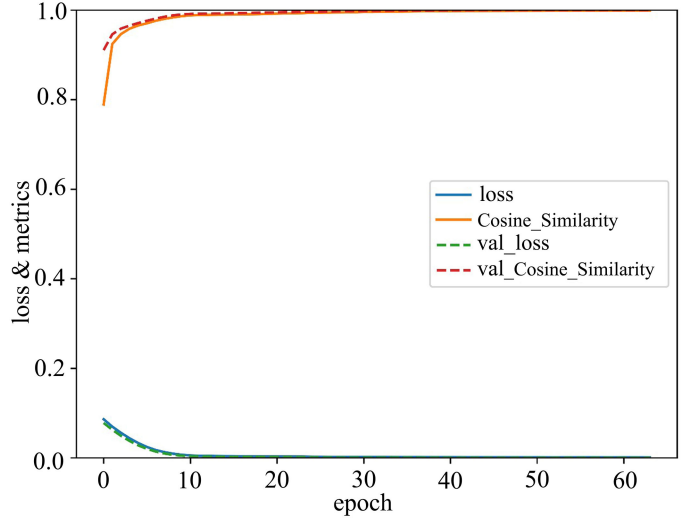

Fig. 5. Loss and metrics performance in training process based on GRU.

calculated as follows:

$$\cos_{\text{sim}(X,Y)} = \frac{\vec{x} \cdot \vec{y}}{\| x \| \cdot \| y \|} = \cos\theta_{xy}. \tag{2}$$

Using the constructed GRU network, the pixel values of InSAR deformation data are compressed sequentially, pixel by pixel. The formula is as follows:

$$F_{i,j} = \begin{cases} \frac{M_{i,j}}{f_{\text{FitMax}}(t)}, & M_{i,j} > 0 \\ \frac{M_{i,j}}{|f_{\text{FitMin}}(t)|}, & M_{i,j} \leq 0 \end{cases} \tag{3}$$

where M_{ij} is the pixel value of the ith row and j column of the image, O_{ij} is the output value of the image after compression, f_{Max} and f_{Min} are GRU fitting value at the current time step, and the range of pixel value after compression is $[-1, 1]$.

b) Inverse normalization of spatiotemporal prediction data: The model predicted a pixel value range of $[-1, 1]$ for the deformation data. To restore the predicted data to their original scale, a GRU fitting value at the current time step constructed above was adopted to multiply the maximum value by a positive value and the minimum value by an absolute value to restore the pixel value of the predicted deformation data to the original scale. The formula is as follows:

$$F_{i,j} = \begin{cases} M_{i,j} \cdot f_{\text{FitMax}}\left(t\right), & M_{i,j} > 0 \\ M_{i,j} \cdot |f_{\text{FitMin}}\left(t\right)|, & M_{i,j} \leq 0. \end{cases} \tag{4}$$

2) Framework of the Spatiotemporal Prediction Model

a) Dataset making: Time-series InSAR deformation data segmentation was used as a sliding window. The time sequence of the original data in this article was short, so the overlapping segmentation method was adopted to ensure the amount of training data. We used the multistep to one-step prediction output mode. The input of the multistep to one-step form was multiple images with the time step as the first dimension, and the label was a single image with the predicted time step. Datasets corresponding to network input and output were prepared before each network training. Before the model started training, InSAR
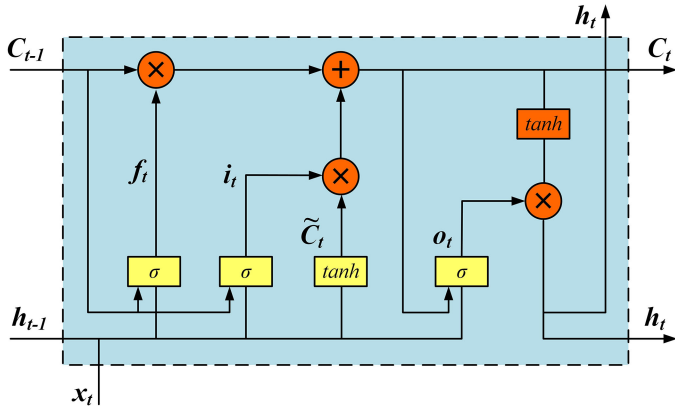
Fig. 6.   Structure of PhLSTM cell.

deformation data were divided into training and testing sets, and the last 20 data were selected for the testing set. The training set accounted for 80% and the validation set for 20% of the rest of the data.

b) Peephole LSTM (PhLSTM) network: Hochreiter and Schmidhuber [43] proposed an LSTM neural network model, which is a type of time-recurrent neural network. Due to its unique design structure, the LSTM neural network is suitable for processing events with long intervals and delays in time series, that is, when the number of network layers increases. Over time, the latter layer becomes less aware of the former layer, and information from the former layer is forgotten. LSTM can effectively simulate the problem of multi-input variables, so it is suitable for time-series processing and prediction [27].

The PhLSTM network is a variant of the LSTM. PhLSTM can learn the fine distinction between spike sequences of spikes spaced either 50 or 49 time steps apart without the help of any short training exemplars [33]. PhLSTM allows output gates to utilize the previous internal state as well as the previous hidden state [44]. The output gate layer also receives the cell state input, and the output gate receives the updated cell state. Each PhLSTM memory unit is composed of an input gate (i), output gate (O), forgetting gate (f), and memory cell (C). Therefore, information processed by a PhLSTM network is more comprehensive and has higher accuracy in time-series prediction. The structure of a single memory unit is shown in Fig. 6. The symbol ⊕ represents the addition operation of two vectors, and the symbol ⊗ represents the dot product operation of two vectors.

The specific calculation process of the PhLSTM cell from input to output can be divided into the following four steps:

Decide to discard information:

$$f_t = \sigma \left(W_f \circ [x_t, C_{t-1}, h_{t-1}] + b_f \right). \tag{5}$$

Confirm update information:

$$i_t = \sigma \left(W_i \circ [x_t, C_{t-1}, h_{t-1}] + b_i \right) \tag{6}$$

$$\tilde{C}_t = \tanh \left(W_c \circ [x_t, h_{t-1}] + b_c \right) \tag{7}$$

Cell state:

$$C_t = f_t \circ C_{t-1} + i_t \circ \tilde{C}_t \tag{8}$$

Output information:

$$o_t = \sigma \left(W_o \circ [x_t, C_t, h_{t-1}] + b_o \right) \tag{9}$$

$$h_t = o_t \circ \tanh \left(c_t \right) \tag{10}$$

where the symbol "∘" represents the Hadamard product operation of two vectors, W_f, W_i, W_o, and W_c represent the weight vectors of forgetting gate, input gate, output gate, and memory unit, respectively, and b_f, b_i, b_o, and b_c represent the offset direction of forgetting gate, input gate, output gate, and memory unit, respectively.

c) Model construction based on time-series InSAR deformation data: In this article, we created an integrated network of coding modules, prediction modules, and decoding modules based on CNN and PhLSTM, called CNN–PhLSTM. First, deep temporal features of the time-series InSAR deformation data were extracted by time-distributed CNN segmentation. Second, deep time-series feature vectors were input into a stacked PhLSTM for time sequence feature value prediction. Finally, the predicted feature vectors, namely spatial data, were restored to raster images, using the alternating stacking method of upsampling and convolution layers, and the spatiotemporal prediction was realized. In this article, the prediction process was multistep to one-step, which was also overlapped and cut. After many experiments, the index was most effective when the input time-step length was five. The specific process is shown in Fig. 7.

In the coding module, the time distribution convolution was constructed to share parameters in each convolution kernel to ensure that each time step was independent to extract deep temporal features. Because there are more convolutional layers, many nonlinear fitting functions can be placed, enhancing the model's fitting ability, and obtaining more global and abstract features. The convolution layer located in maximum size the feature graph has a convolution kernel size of 450×450, which subsequently decreases to 225, 75, 25, 5, and 3. The convolution layer's output channel increases as the feature graph size decreases and the convolution layer's output channel located in the maximum size feature graph is one. In the end, the convolution layer's output channel increases to 32, 64, 128, 256, and 512. Global average pooling is applied to transform feature graphs into vectors.

In the prediction module, three PhLSTM layers were used to capture time-series features in the temporal direction for prediction, and predictive feature vectors were obtained. The deep time-series features were input into a stacked PhLSTM for time sequence feature value prediction. The output units were 512, 256, and 128, respectively. The last PhLSTM layer returned only the state of the last cell, not the sequence, and the output prediction module was only of the last cell.

In the decoding module, we transformed a single feature vector into a specific dimension matrix using a reshape function. Based on five gradually expanding dimensions, we gradually restored the dimensions and feature details by stacking the time-distributed convolution and upsampling layers. The convolution kernel size of the convolution layer connected behind each upsampling layer was the same as the upsampling factor to reduce the hard-edge problem caused by the nearest neighbor
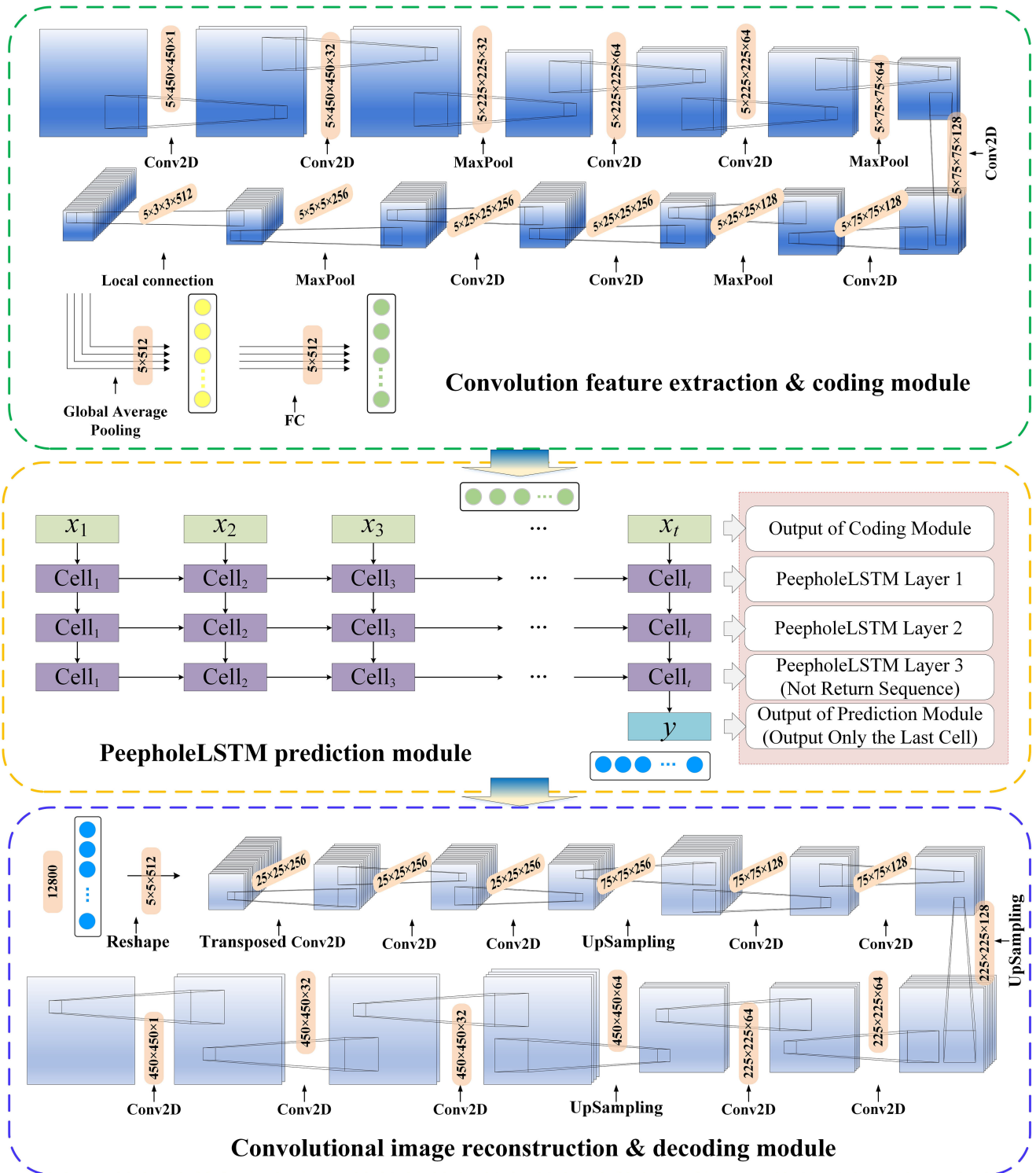
Fig. 7. Spatiotemporal prediction network structure of CNN–PhLSTM.

algorithm in the upsampling layer. The convolutional layer's output channel decreased as the size of the feature graph increased, and 256 convolutional layers, whose output channels were gradually reduced to 1 were used to reconstruct the data. Finally, the predicted feature vectors, namely spatiotemporal prediction data, were restored to the raster images.

The convolution calculation output value usually needs to achieve nonlinear transformation through the activation function, and rectified linear unit was chosen as the activation function. In the spatial predicted value of output data in the CNN–PhLSTM model training process, the loss function for each pixel was the mean absolute deviation (MAE), the loss

function for whole image was the multiscale structural similarity (MS-SSIM), and the optimizer was updated by adaptive motion (Adam) estimation [45]. This process was repeated through multiple epochs until the loss function approximately converged to the minimum value and the model achieved the desired effect. The time step is 15, epoch is 256, train batch size is 4, and learning rate is 5×10^{-4}.

The self-defined loss function is the sum of the weights of MAE and MS-SSIM, and its expression is as follows:

$$\text{Loss} = W_{\text{MAE}} \times \text{MAE} + W_{\text{MS\_SSIM}} \times (1 - \text{MS} - \text{SSIM}) \tag{11}$$

where W_{MAE} and $W_{\text{MS·SSIM}}$ are the weights of MAE and multiscale structure similarity, respectively, which are set as $W_{\text{MAE}} = 0.7$ and $W_{\text{MS·SSIM}} = 0.3$ in this experiment.

3) Evaluation Index

To quantitatively assess the performance of the model, the mean squared error (MSE), MAE, SSIM, and peak signal-to-noise ratio (PSNR). indicators are used to evaluate the results of the model prediction output.

MSE can be expressed as

$$\text{MSE} = \frac{1}{m} \sum_{i=1}^{m} (y_i - \hat{y}_i)^2 \tag{12}$$

MAE can be expressed as

$$\text{MAE} = \frac{1}{m} \sum_{i=1}^{m} |y_i - \hat{y}_i| \tag{13}$$

SSIM can be expressed as

$$\text{SSIM} (x,y) = \frac{\left[2\mu_x \mu_y + (k_1 L)^2 \right] \left[2\sigma_{xy} + (k_2 L)^2 \right]}{\left[\mu_x^2 + \mu_y^2 + (k_1 L)^2 \right] \left[\sigma_x^2 + \sigma_y^2 + (k_2 L)^2 \right]} . \tag{14}$$

The above three formulas are image brightness, contrast, and structure, respectively, where μ_x and μ_y are the mean values of the two images, σ_x and σ_y are the standard deviations of the two images, σ_{xy} is the covariance of the two images, L is the dynamic range of pixel values, k_1 and k_2 are two scalar constants, and $k_1 = 0.01$ and $k_2 = 0.03$ by default. The SSIM of two images is generally defined as follows:

MS-SSIM:

$$\text{M S}_{\text{SSIM}(x,y)} = [l_M (x,y)]^{\alpha_M} \prod_{j=1}^{M} [c_j (x,y)]^{\beta_j} [s_j (x,y)]^{\gamma_j} . \tag{15}$$

M was the highest scale (the original image scale was 1, and the scale increased by 1 after low-pass filtering and downsampling twice). MS-SSIM only calculated the brightness comparison at the highest scale, and the default values of the importance parameters α_M, β_j, and γ_j at different scales were adopted ($\beta_1 = \gamma_1 = 0.0448$, $\beta_2 = \gamma_2 = 0.2856$, $\beta_3 = \gamma_3 = 0.3001$, $\beta_4 = \gamma_4 = 0.2363$, and $\alpha_5 = \beta_5 = \gamma_5 = 0.1333$).

PSNR can be expressed as

$$\text{PSNR} = 10 \times \log_{10} \left[\frac{(2^n - 1)^2}{MSE} \right] . \tag{16}$$
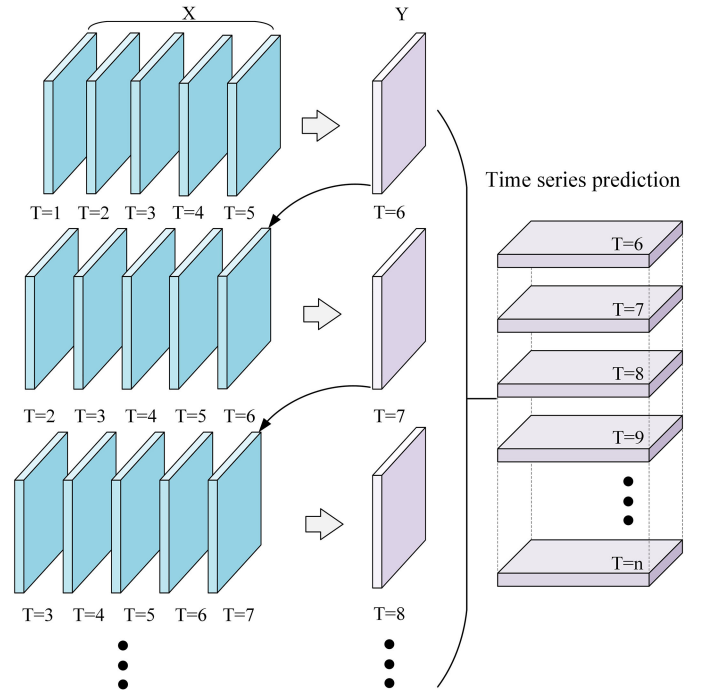

Fig. 8.   Specific prediction process of time-series data.

4) Predictive Simulation Based on the Proposed CNN–PhLSTM

The operating environment selected in the experiment is shown in Tables I and II.

Based on the proposed CNN–PhLSTM model, we set the InSAR deformation grid data as $X = \{X_T\}$, $T = 12,3 \dots, N$, where X and Y are input and prediction data, respectively.

The iterative backward prediction model was adopted for the area prediction process, that is, Y obtained from the previous time-series data prediction was added to the input dataset to form a new time-series deformation dataset X. The specific prediction process is shown in Fig. 8.

IV. RESULTS AND ANALYSIS

A. Characteristics of Surface Deformation in 2014–2021

We used ArcGIS software to draw the LOS direction spatial distribution of surface deformation rates (Fig. 9) in the Jinchuan mining area based on Sentinel-1A data from October 2014 to April 2021. Fig. 8 shows three continuous subsidence areas, namely the Longshou, second western, and third eastern mining areas. The second western mining area had the largest average annual subsidence rate, and the average annual deformation rate was −171.17–14.42 mm. The surface deformation rate in the third eastern mining area was slower than other two mining areas. Fig. 9 shows that the surface deformation of second western mining area was along different slopes, while that of the Longshou mining area was along the same slope, and the slope value was large in the Longshou mining area.

TABLE I
BASIC SYSTEM PLATFORM CONFIGURATION

Project	Operating system	CPU	Memory	Disk	GPU
Content	Microsoft Windows 11 Pro Insider Preview Build 25163	AMD Ryzen 9 4900HS with Radeon Graphics	DDR5 16GB 3200MHz	Intel 660P M.2 80mm (1TB)	NVIDIA GeForce RTX 2060 with Max-Q Design GDDR6 @ 6GB (192 bits)

TABLE II
IMPORTANT SOFTWARE (PACKAGE) CONFIGURATION

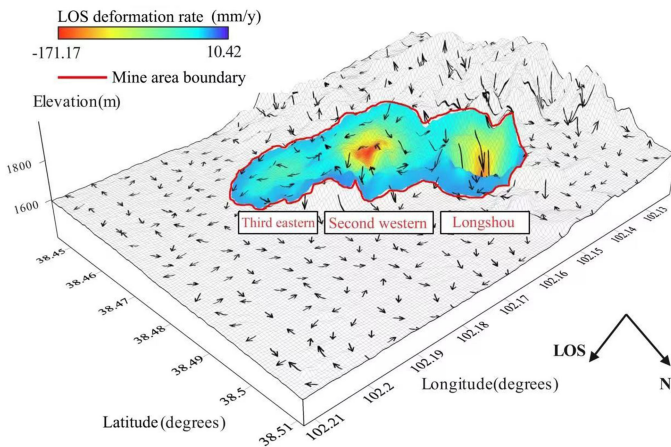| Project	Graphics driver	CUDA	CUDNN	Python	Keras	TensorFlow	Scikit-learn
Content	516.40 GRD	V11.2.152	V8.1.1.33	3.10.5	2.9.0	2.9.1	1.1.1

Fig. 9. Spatial distribution of LOS direction surface deformation rate in Jinchuan mining area (arrow indicates aspect and arrow length indicates slope).

Fig. 10 shows the spatial variation of accumulated surface deformation in the Jinchuan mining area from October 14, 2014 to April 16, 2021. In addition, there was a surface uplift area on the east side of the Longshou mining area, and over time it expanded, and the cumulative uplift increased. Because of the particularity of repeated mining, the displacement of rock and soil mass also increased. Displacement caused by activation deformation is significant, and finally led to the rise of the bottom of Longshou open-pit mining [46]. Fig. 10 shows the west-second mining area over the same time period, during which the surface deformation area expanded, cumulative surface deformation increased, and final cumulative settlement reached 1.17 m. The accumulated settlement of second western mining area increased rapidly and the spatial expansion accelerated. The deformation boundary range of the third eastern mining area also expanded time, but it remained stable and invisible from August 2020 to April 2021.

In order to further analyze the evolution of surface deformation in the Jinchuan mining area, surface displacement curves for profiles I, II, and III were drawn, as shown in Fig. 11(a). Fig. 11(b) shows the plotted change process of curve I in different periods. It crossed three mining areas simultaneously in a northwest to southeast direction. According to the profile line trends, the profile deformation curves along the north-southeast direction in the three settlement areas conform to the Peck formula [47], indicating that surface subsidence was caused by construction. The second western mining area had the largest deformation and the maximum negative movement was −1167 mm. Fig. 11(c) and (d) shows the Longshou and second western mining area profiles. With the mining of the working panel, the surface subsidence along the profile increased continuously and the spatial distribution expanded continuously, but the east end of the Longshou mining area was uniformly uplifted. As can be seen from the profile lines in Fig. 11(b)–(d), the interval of accumulated subsidence curves of each phase during 2015–2017 decreased, indicating that the subsidence rate slowed. The interval of accumulated subsidence curves from 2018 to 2021 was approximately equal, implying that the deformation area had uniform subsidence in the last 3 years.

B. Evolution Trend of Surface Deformation During 2021–2024

Based on the spatial and temporal distribution of InSAR deformation data, our proposed CNN–PhLSTM model was used to predict the spatiotemporal evolution trend of surface deformation in the Jinchuan mining area from April 28, 2021 to April 12, 2024, and ArcGIS software was used to draw the spatiotemporal distribution map.

Fig. 12 shows the surface deformation rate of the Jinchuan mining area in 2022 and 2023. In 2022, the average annual surface deformation rate was predicted to be −78.17–6.59 mm [Fig. 12(a)]. In 2023, the average annual surface deformation rate was predicted to be −64.24–7.13 mm [Fig. 12(b)]. The analysis predicted that the deformation rate in 2023 would be
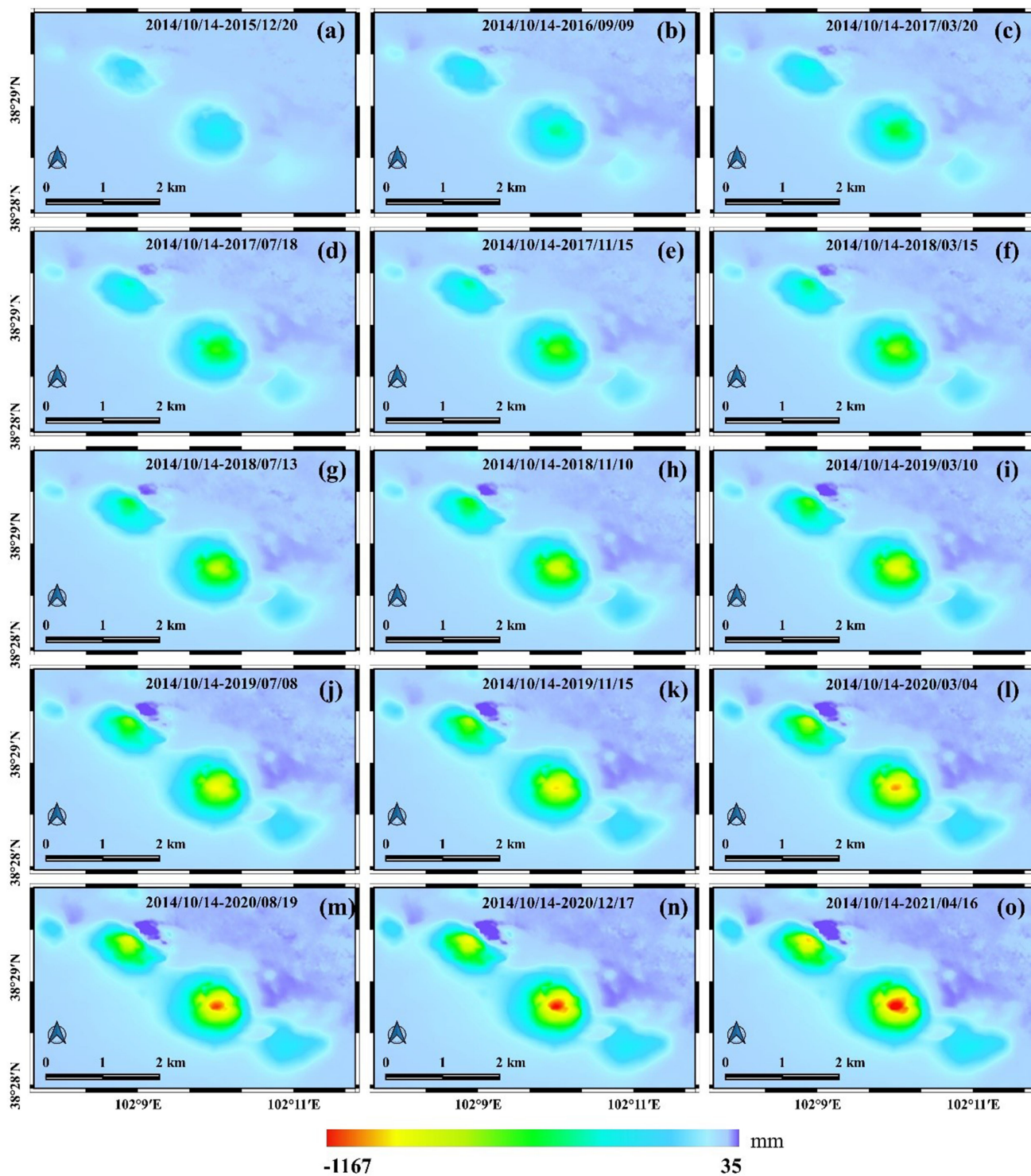
Fig. 10. Spatiotemporal distribution of LOS accumulated surface deformation.

slower than that in 2022. To test and verify the rationality of these predictions, we used uniform sampling to select test points in the deformation area, using the location distribution as show in Fig. 13(a), to draw test points on the accumulated subsidence curve as shown in Fig. 13(b). The results show that surface of the Jinchuan mining area as a whole is predicted to have the uniform

subsidence tendency in the next 2 years, and the subsidence rate will vary in different regions.

The Jinchuan mining area surface deformation range will continue to expand in the future, and temporal accumulative deformation will continue to increase until April 2024 (Fig. 14). The deformation of second western mining area will reach
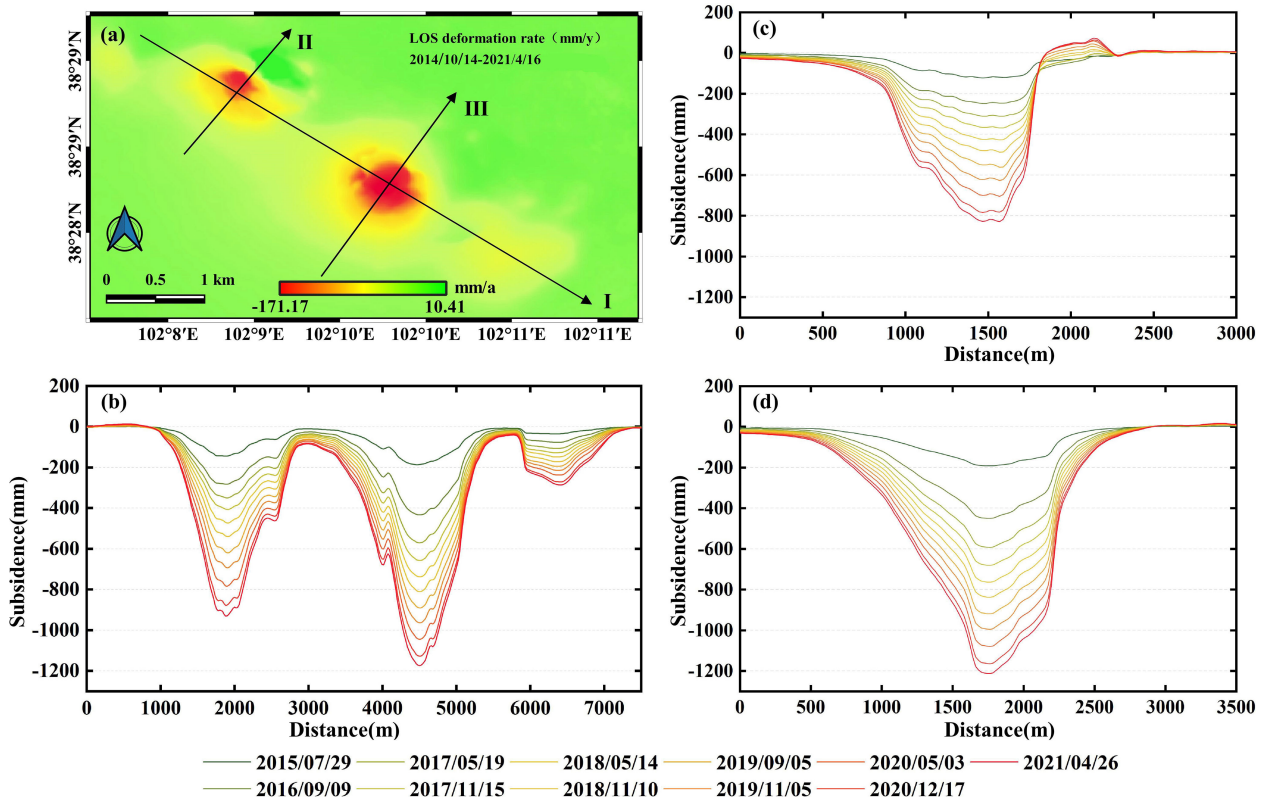
Fig. 11. Cumulative surface deformation of different profiles in Jinchuan mining area. (a) Surface displacement curves for profiles I, II, and III. (b) Subsidence of curve I in different periods. (c) Subsidence of curve II in different periods. (d) Subsidence of curve III in different periods.
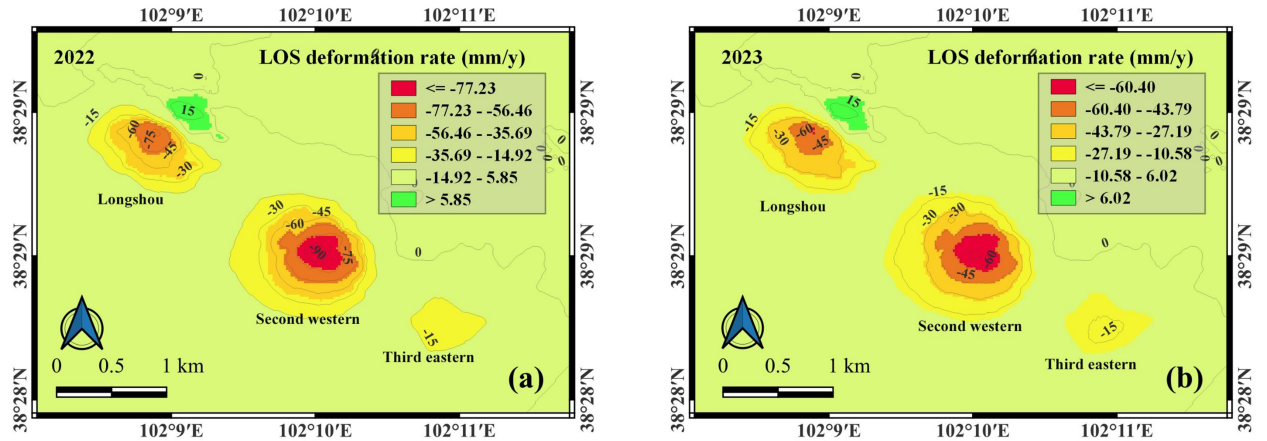

Fig. 12. Surface deformation rate of Jinchuan mining area in 2022 and 2023.

−1500 mm. The spatial distribution diagram of each time period shows that temporal surface deformation will continue as uniform subsidence in the future.

V. DISCUSSION

A. Precision Analysis of InSAR Surface Deformation Results

The accuracy of the InSAR surface deformation results is the key to the analysis and predictive simulation of spatiotemporal characteristics in the Jinchuan mining area. The precision analysis methods for the InSAR deformation results include

comparisons with benchmark data [48], InSAR deformation results from different data sources [49], the different InSAR technology results [13], and existing regional-scale research results in study area. In this article, the benchmark data [38], InSAR deformation results of different orbits data [50] in the existing literature, and existing research results are compared to and verified using the InSAR deformation results of this article; then, the accuracy is analyzed.

1) Comparison and verification with the benchmark data in the existing literature: The benchmark data in April 2014–February 2017 [38] were used to select benchmarks
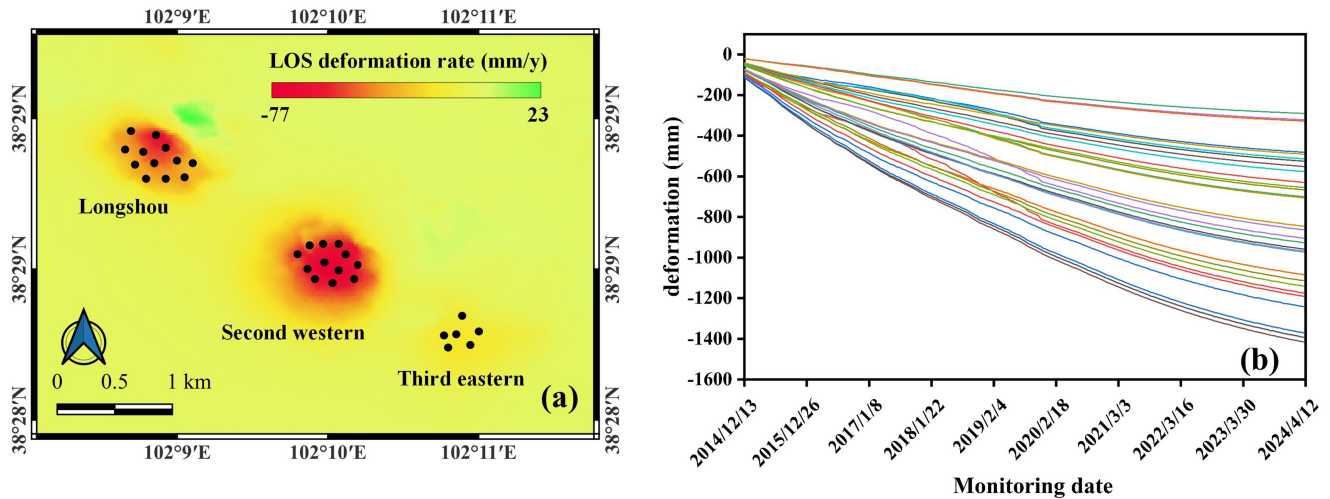
Fig. 13.   Position and deformation curve of test points.

with clarity and good integrity (Fig. 1) to verify the InSAR measurement deformation results from this article. The benchmark data recorded the monthly cumulative vertical deformation value of the point. InSAR measurement results were LOS deformation. Therefore, the LOS InSAR measurement results were converted to vertical direction results for verification. The study area is small and the Sentinel-1A incidence angle changes very little, we convert LOS (d_{LOS}) into vertical displacement (dv) for every time series using the Sentinel-1A incidence angle ($\theta = 34.17°$): $dv = d_{\mathrm{LOS}}/\cos\theta$ [51].

Specifically, we extracted SBAS–InSAR timing vertical deformation vector monitoring points from the same period in a circular buffer with a 20-m radius from the horizontal point position, calculated their average, and compared the InSAR deformation results with benchmark values. As seen in Fig. 15(a), the InSAR results at benchmarks showed a consistent trend with the benchmark results. The error range of comparison with the benchmark was 0–8 mm. Both met the requirements for measuring of ground movement. This indicates that the SBAS–InSAR monitoring results have a high consistency with the benchmark results, which proves that the experimental parameters set in this article are reasonable and that the InSAR deformation results are reliable.

2) Comparison and verification with InSAR measurement data of different orbits: By comparing this article's InSAR measurement vertical results with existing research results, Yang et al. [50] analyzed the 3-D characteristics of Jinchuan mining area using multiple orbits, and conducted correlation analysis of InSAR measurement vertical results of different orbits in the overlapping period [Fig. 15(b)]. We found that the correlation coefficient between this article's InSAR measurement results and the existing InSAR measurement vertical results of different orbits is 0.68. This again proves the reliability of the InSAR measurement results in this article and can be used as the data basis for spatiotemporal characteristics and predictive simulation.

3) Comparison and verification with existing regional-scale research results in study area: Based on Sentinel-1A data from October 2014 to October 2017, Geng et al. [35] obtained the time-series deformation of Longshou mining area by using SBAS–InSAR technology, and the research results were in good agreement with our research. Based on Sentinel-1A data from January 2016 to November 2019, Li et al. [36] obtained the time-series deformation of second western mining area by using SBAS–InSAR technology, and the research results are also in good agreement with the results of this article. It further indicates that the InSAR measurement results of this article are reliable.

B. Analyses of Surface Deformation Mechanisms

Surface stress changes, spatial distribution of faults, and structural strength of lithology caused by mechanized mining are generally the key factors of surface deformation in mining areas [35]. Therefore, this article will analyze the mechanism of surface deformation in the Jinchuan mining area using three factors, man–machine mining, faults distribution, and lithology structure, as follows:

1) Relationship between surface deformation and man–machine mining: Minerals from underground mining, the ore room inside and around the stress state of instability, stress balance, in order to achieve coverage over the mining area of strata and surface feature under the action of gravity, rock masses will be out of shape, which mainly show as collapse, fracture, and fold forms, which in turn deform the ground [52]. This deformation forms the subsidence funnel, which is centered on veins. With orderly mining development, the deformation of the Jinchuan mining area tends to be stable. Underground mining activities likely caused the original movement and deformation of the slope rock mass under open-pit excavation condition. When the activation was greater than the subsidence caused by underground mining, the bottom of the open-pit mine would be pushed up [46]. Therefore, one cause of

2022-08-21

2022-12-19
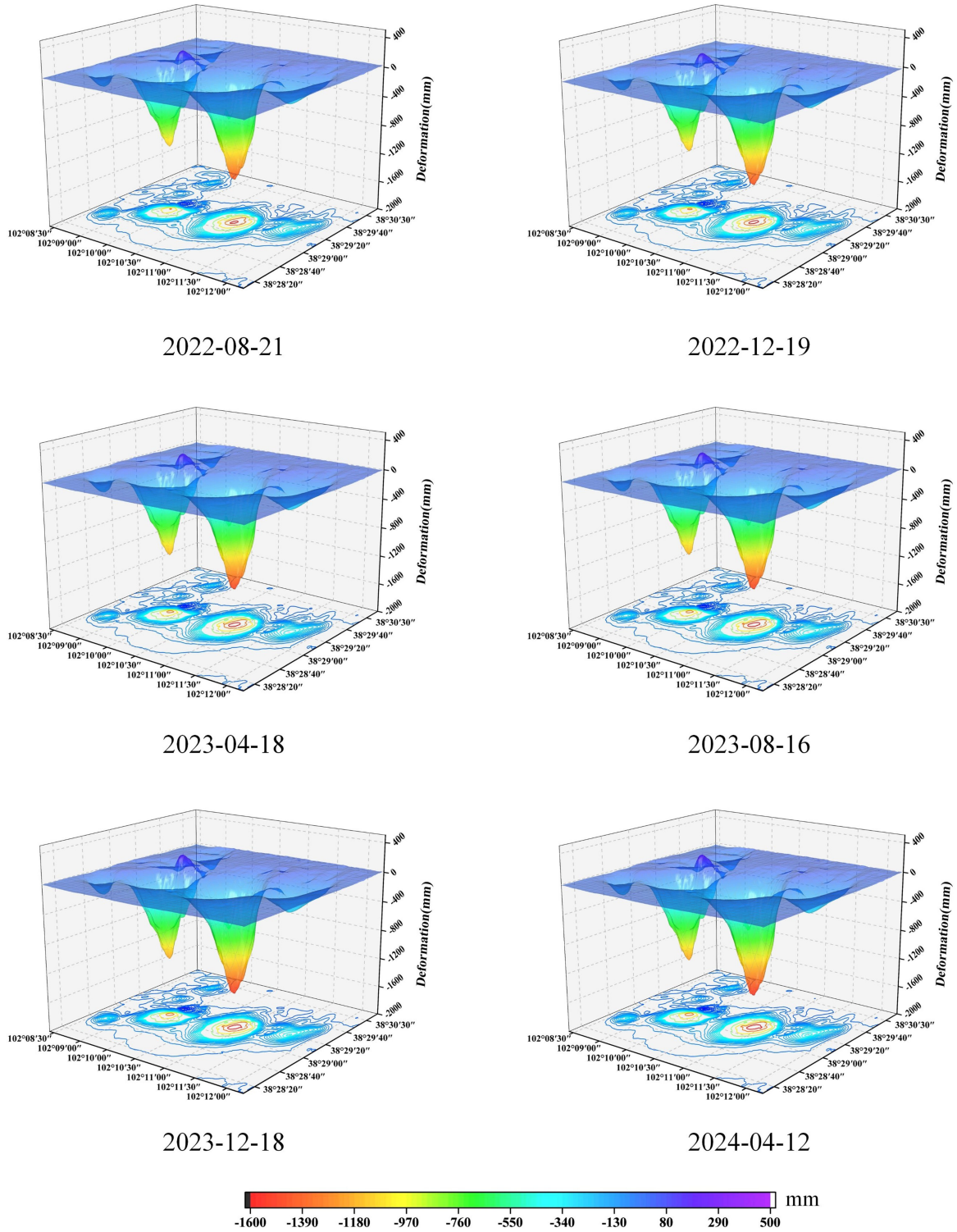
2023-04-18

2023-08-16

2023-12-18

2024-04-12

Fig. 14. Accumulated deformation distribution of Jinchuan mining area in the future.

surface deformation in the Jinchuan mining area from 2014 to 2021 may be man–machine mining.

2) Surface deformation and the relationship between faults: As shown in Fig. 16(a), the Jinchuan mining area north of the F1 fault zone is divided into upper and lower plates. The upper plate mainly includes Proterozoic

metamorphic rock and upper Paleozoic sedimentary rocks. The rocks have multigenerational ultrabasic dyke intrusions and form the Dragon Mountain orebody [53]. The footwall rock series mainly includes Jurassic to Tertiary continental clastic sedimentary rocks [38], [54]. Despite the mining going on, the hanging wall does not show
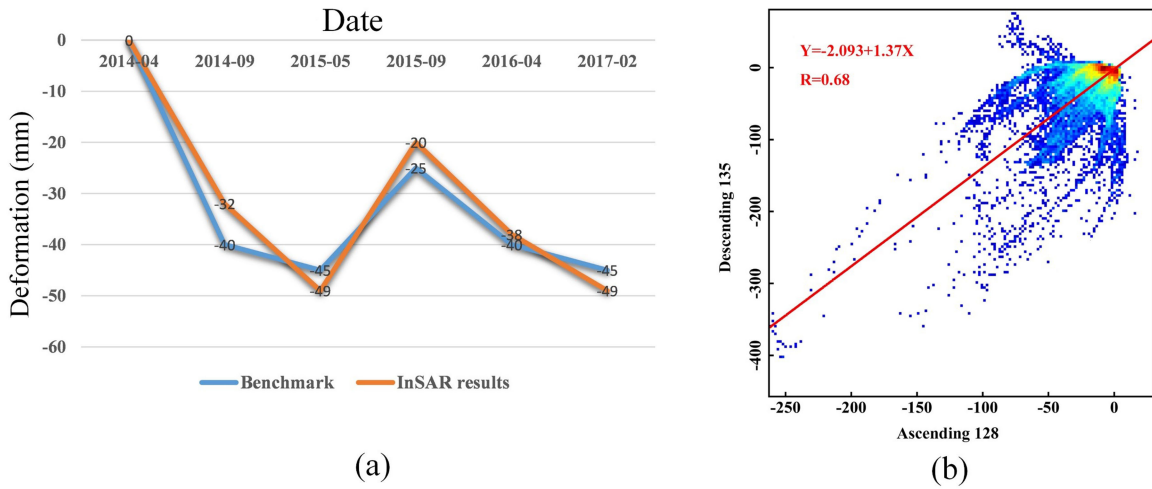
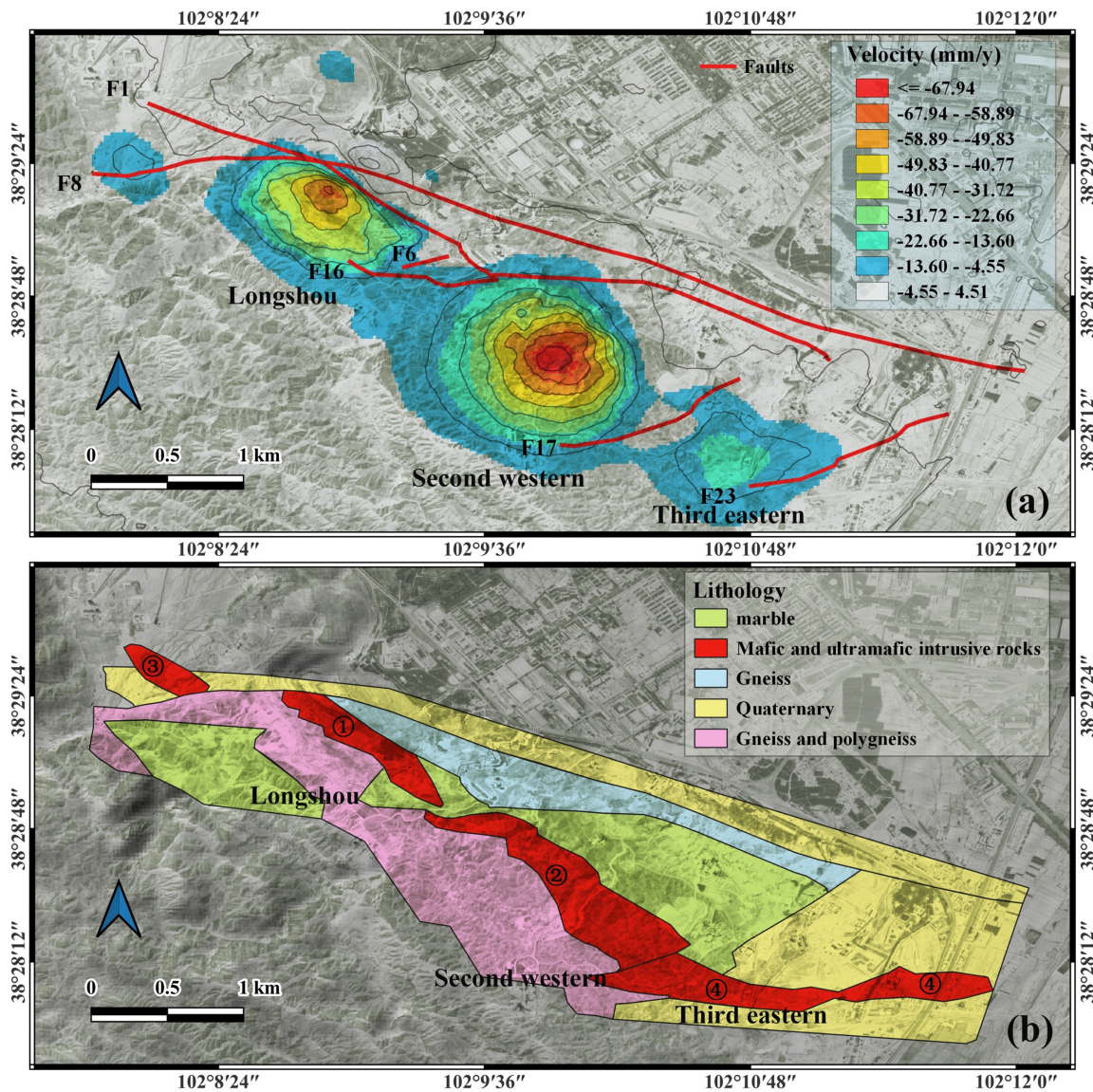Fig. 15.   Precision analysis of InSAR surface deformation results.

Fig. 16.   Distribution of faults and lithology structure.

obvious subsidence due to the influence of the F1 fault. It intersects the F16, F17, F23, and F1 faults, which are distributed alternately with ore bodies. The dip angle varies from 60° to 80°, which divides the rock mass into three parts, Longshou, second western, and third eastern mining areas. Therefore, the Jinchuan mining area overall shows three continuous subsidence areas. The F8 and F6 faults are north of the Longshou mining area. The deformation area monitored by InSAR appears discontinuous on the boundary of this fault. In Fig. 10(c), the sharp increase of subsidence near 1000 m is the result of the cross-cutting F6 fault. The southwest is controlled by the F3 fault, and the subsidence of the whole mining area is limited to an approximate ellipse under the action of the F3 fault. North second western mining area in addition to the distribution of F16 fault no around the main fault exists, so the exploration area centered on veins form of approximate circular settlement expansion to the surrounding area constantly, but still is limited by the fault in northern expansion of the scope. We predict that in the process of ongoing mining, in addition to the northern area under fault control, the subsidence area will continue to expand. The third eastern mining area is controlled by the F17 and F23 faults, and the subsidence area is confined to area between of the two faults, forming a semicircle distribution. According to the above analysis, the fault distribution in the Jinchuan mining area controls the spatial distribution of surface deformation [55].

3) The relation between surface deformation and lithology: The lithology of the Jinchuan mining area is complex, and regional differences are great [Fig. 16(b)]. The northeastern parts of the Longshou and second western mining areas are the gneiss group, which is mainly composed of dolomite and calcite. The particles are uniform and fine, the texture is uniform, the hardness and structural strength are low, and deformation easily occurs under stress and erosion [13], [56]. In the southwest, there are gneisses and compound gneisses, which are mainly composed of feldspar, quartz, mica, etc., and also include amphibole and pyroxene. They exhibit uneven grain size, and texture, as well as high overall structural strength. Affected by continental temperate arid climate and surface lithology, the Jinchuan mining area surface formed a soft, thick layer of loess mixed with sand, gravel, clay, and loose accumulation. The surface's overall density is low with poor structural strength. Long-term erosion by rain and seepage reduced the cohesive strength of the loess, clay, sand, and matrix suction, and destroyed the steady-state accumulation. The overburdened sand softened and stability decreased [51], [57], and [58], resulting in the collapse of the artificial building foundation in the mining area and the deformation of the overburden surface. Surface deformation of the Jinchuan mining area will continue with manual mining. The stability of the rock mass in the western mining area is greater than that in the eastern mining area [38]. With the multistage invasion of mafic and ultramafic intrusive rock and ultrabasic rock, joint and
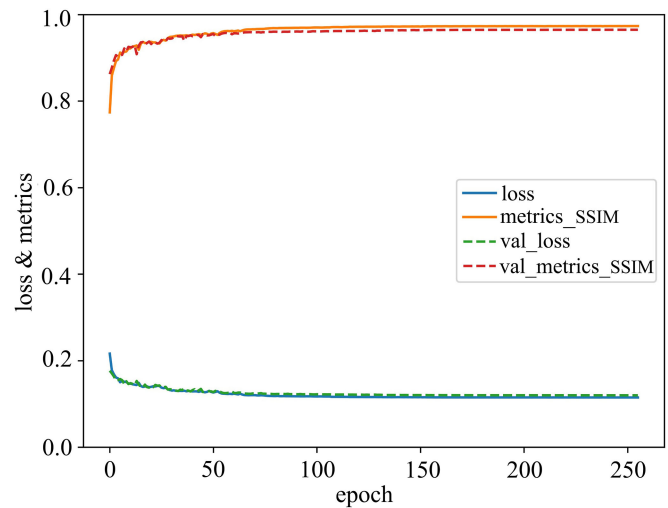

Fig. 17. Training and testing curve of the proposed CNN–PhLSTM model.

fracture development is broken, so the subsidence of the eastern mining area will be more obvious. In summary, lithology is another controlling factor of surface deformation in the Jinchuan mining area.

C. Performance Analysis of the Proposed Method

The proposed prediction model is influenced by several hyperparameters, such as the number of network layers, learning rate, number of hidden layer units, and training times, of which sample partition length (length of history sequence), number of network layers and number of hidden layer units are the most critical factors. The trial-and-error method was used to debug the hyperparameters, and the optimal hyperparameters were obtained after several rounds of debugging. The sample partition length (length of historical sequence) was 5, the number of PhLSTM network layers was 3, and the number of hidden layer cells was 256 and 128. Meanwhile, the CNN–PhLSTM prediction model was obtained using these hyperparameters' training. As seen in Fig. 17, during model training, the change of loss function (loss) converged normally, and overfitting in network training was effectively suppressed. After 64 epoch complete iterations of the training set, the network finally converged, and the many steps to one step network model with different time steps obtained approximately 0.85–0.92 SSIM on the training set. An SSIM of approximately 0.84–0.90 was obtained from the test set (Fig. 17). The SSIM converts the image of multiple time steps into multiple channels of a single image for calculation. Therefore, the spatiotemporal prediction model trained in this article is an effective model.

In order to more accurately evaluate the proposed model's reliability, we analyzed the changing trends of the minimum and maximum values of the original data and predicted data within the time series (Fig. 18). The above numerical change curves significantly overlap in the training and verification sets, and the errors in the test set are relatively small. The subsequent time series trend is consistent with that of the original dataset. In addition, the errors in the test set may be related to our
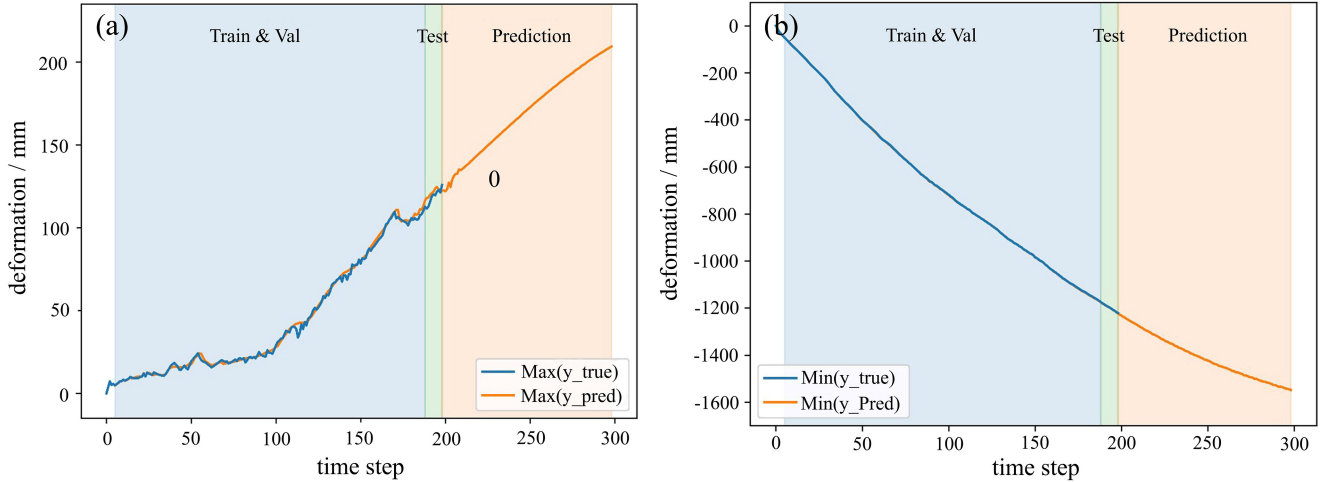
Fig. 18.   Variation trend of maximum and minimum values of raw and predicted data.

TABLE III
COMPARISON OF MULTIPLE INDICATORS OF DIFFERENT MODELS

Models	Error					Time
	MAE	MSE	SSIM	MS-SSIM	PSNR	
SVR	3.7414	171.1836	0.9878	0.9979	39.9095	2h53min15s
MLP	2.6725	107.0679	0.9868	0.9981	42.3854	12h10min26s
CNN-LSTM	1.5269	7.9471	0.9942	0.9993	53.9144	2h37min59s
Proposed model	1.4236	7.3777	0.9949	0.9995	54.4293	3h48min37s

interpolation of SBAS–InSAR inversion results because there are empty time steps in the test set.

Additionally, we randomly selected real InSAR deformation data and corresponding simulated prediction data from October 18, 2020; December 17, 2020; February 15, 2021; and April 16, 2021, and calculated their correlation using the Pearson correlation calculation method (Fig. 19). The real InSAR deformation diagram fits well with the predicted deformation diagram, and the maximum R^2 is 0.9981.

In order to further verify the performance of the proposed model, the support vector regression (SVR), multilayer perceptron (MLP) and CNN–LSTM models, and five evaluation indicators were mainly selected (Table III). It can be seen from Table III that the proposed model is the best among all the evaluation indicators, with the largest difference in MSE values. The MSE values of the traditional SVM and MLP models are large, while the MSE values of CNN–LSTM and the proposed model are small, but the proposed model has the smallest MSE value, indicating that the proposed model is the best and has the highest prediction accuracy.

We calculated the running time of each model, the time of SVR and MLP models were the slowest, CNN–LSTM model was faster than CNN–PhLSTM model, because LSTM was specially optimized by TensorFlow on NVIDIA's CUDA, while PhLSTM did not have this optimization. After CUDA optimization, the adjustment of some hyperparameters of LSTM was limited, so CNN–LSTM algorithm must be the fastest. In

fact, the efficiency of CNN–LSTM and the proposed model should be about the same theoretically.

However, the proposed model had the highest accuracy because LSTM is no direct connection from the CEC (constant error carousel), all it can observe directly is close to zero as long as the output gate is closed, and the resulting lack of essential information may harm network performance [59]. The PhLSTM network to add weighted "peephole" connections from the CEC to the gates of the same memory block. PhLSTM allows output gates to utilize the previous internal state as well as the previous hidden state. The output gate layer also receives the cell state input, and the output gate receives the updated cell state [44]. Therefore, information processed by a PhLSTM network is more comprehensive and has higher accuracy in time-series prediction. Therefore, the proposed model has good performance and the highest prediction accuracy.

D. Research Limitations and Future Prospects

In this article, the spatiotemporal evolution characteristics of surface deformation in the Jinchuan mining area were analyzed using SBAS–InSAR and the future spatiotemporal evolution trend of surface deformation was predicted using the proposed CNN–PhLSTM network model. Compelling results were achieved, but there were some limitations in this article, including the following:

1) The spatiotemporal evolution characteristics of the mining areas lack a 3-D analysis. In this article, only LOS InSAR
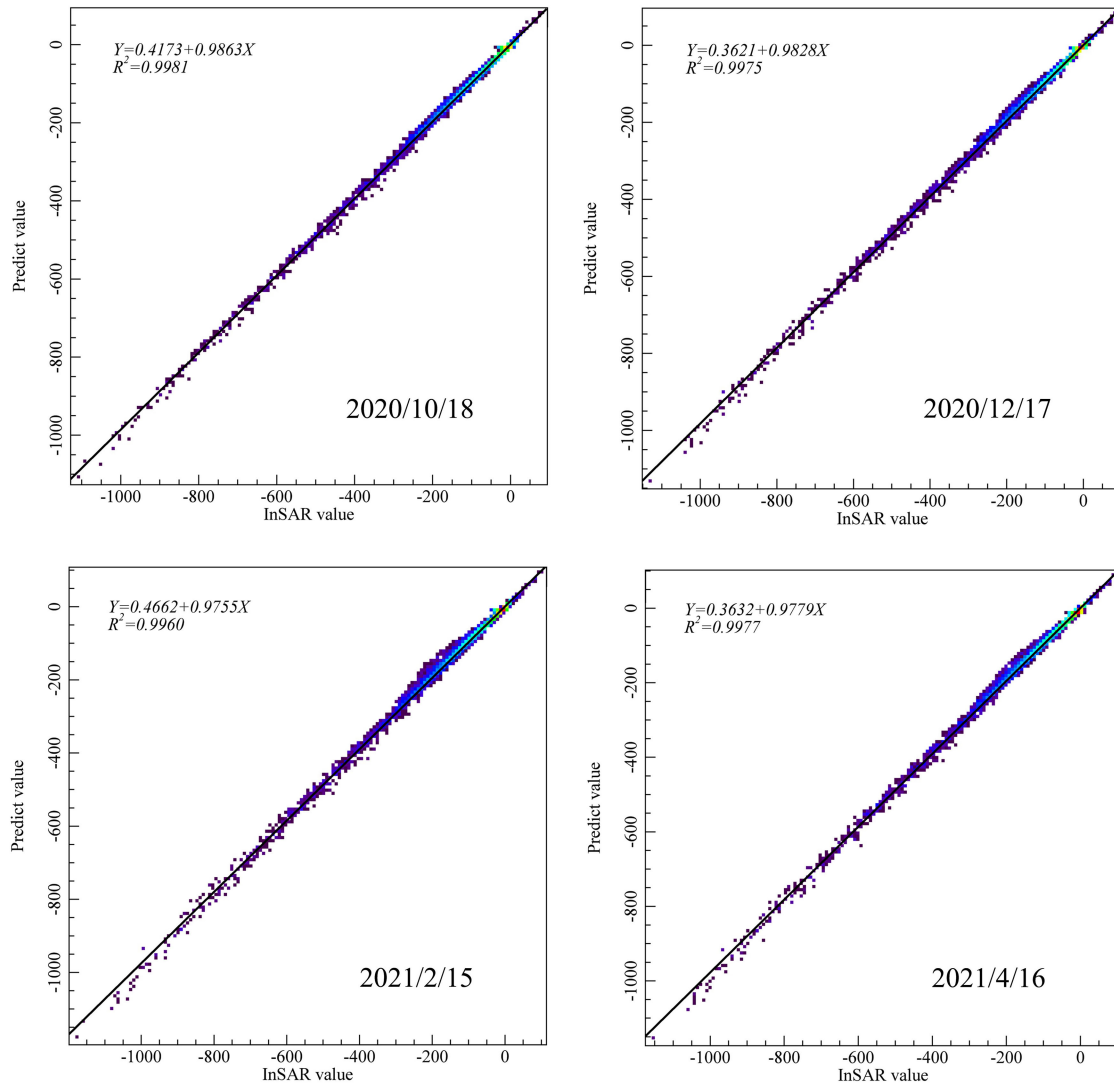
Fig. 19. Correlation between InSAR measured and predicted values.

deformation results were systematically analyzed, ignoring the spatial and temporal characteristics of east–west and north–south deformations.

2) Quantitative mechanism analysis is lacking. Due to data limitations, the spatiotemporal evolution of surface deformation in the Jinchuan mining area is only discussed qualitatively as a mechanism.

3) The proposed prediction model can accurately simulate and predict the spatiotemporal evolution trend of the Jinchuan mining area, but the prediction time scale is limited to only the next 2 years. In addition, the proposed model can only predict the continuous deformation, but not the sudden collapse.

Therefore, in future article, we will first process multiple orbit data, build a 3-D decomposition model, and systematically analyze the spatiotemporal evolution characteristics of the east–west and south–north mining areas, to reveal the evolution of the Jinchuan mining area more accurately. Then we will collect more data to quantitatively analyze the deformation mechanism of the mining area. In addition, compared with deep learning

methods, the newly proposed model is improved as much as possible to heighten model prediction accuracy and extend the model prediction time-scale problem.

VI. CONCLUSION

We used SBAS–InSAR to evaluate surface stability in the Jinchuan mining area based on Sentinel-1A data from 2014 to 2021. The InSAR measurement results in this article were verified by the measured benchmark data and the InSAR measurement data of different orbits. Spatiotemporal laws and mechanisms of surface deformation were analyzed and discussed. The Sentinel-1A InSAR result demonstrated three continuous subsidence areas, namely the Longshou, second western, and third eastern mining areas in the Jinchuan Mine. Of these, the second western mining area had the highest average annual subsidence rate and settlement range. Its average annual deformation rate was −171.17–14.69 mm, its cumulative surface deformation kept increasing and the final cumulative subsidence reached 1.17 m from 2014 to 2021. The subsidence rate slowed down during

2015–2017, but was uniform from 2018 to 2021. We explored the surface deformation mechanism, man–machine mining, fault distribution, and lithology structure three aspects. The results showed that faults distribution and lithology structure were the main causes of surface deformation in the Jinchuan mining area.

We created an integrated network of information considering spatial and time-series InSAR deformation data based on CNN and PhLSTM to predict future spatiotemporal evolution trends of surface deformation, namely, the CNN–PhLSTM. First, time-series InSAR deformation data were compressed using GRUs, and then deep time-series features were extracted by time-distributed CNN segmentation. Next, deep time-series feature vectors were input into a stacked PhLSTM to obtain time sequence feature prediction values. Finally, the predicted feature vectors were restored to raster images by the alternating stacking method of upsampling and convolution layers. Surface deformation for the next 2 years has been predicted by the proposed CNN–PhLSTM model in the Jinchuan mining area. The proposed model was evaluated using SSIM, the consistency of minimum and maximum values in raw and predicted data, and the correlation of the real InSAR deformation data and corresponding simulated prediction data. The surface deformation range is predicted to continue expanding and the time series surface deformation will continue to increase until April 2024, when the surface deformation of second western mining area is predicted to reach -1500 mm. The time-series surface deformation rate is predicted show a slow deceleration trend over the next 2 years.

REFERENCES

[1] J. Kim et al., "Underground burning of Jharia coal mine (India) and associated surface deformation using InSAR data," *Int. J. Appl. Earth Observ. Geoinf.*, vol. 103, 2021, Art. no. 102524.

[2] *CGS: National Mine Geological Survey Report*. Beijing, China: China Geological Survey, 2016.

[3] C. Kuenzer et al., "Geomorphology of coal seam fires," *Geomorphol. Amsterdam*, vol. 138, pp. 209–222, 2012.

[4] G. Modeste et al., "Time evolution of mining-related residual subsidence monitored over a 24-year period using InSAR in Southern Alsace; France," *Int. J. Appl. Earth Observ. Geoinf.*, vol. 102, 2021, Art. no. 102392.

[5] H. Siriwardane et al., "Analysis of subsidence caused by underground mining," *Int. J. Mining Eng.*, vol. 2, no. 4, pp. 271–290, 1984.

[6] L. Nie et al., "A new prediction model for mining subsidence deformation: The arc tangent function model," *Natural Hazards*, vol. 75, no. 3, pp. 2185–2198, 2015.

[7] X. Hui et al., "Monitoring and statistical analysis of mine subsidence at three metal mines in China," *Bull. Eng. Geol. Environ.*, vol. 78, pp. 3983–4001, 2019.

[8] B. Chen et al., "Three-dimensional time-varying large surface displacements in coal exploiting areas revealed through integration of SAR pixel offset measurements and mining subsidence model," *Remote Sens. Environ.*, vol. 240, 2020, Art. no. 111663.

[9] D. Massonnet et al., "Radar interferometry and its application to changes in the earth's surface," *Rev. Geophys.*, vol. 36, no. 4, pp. 441–500, 1998.

[10] M. Jiang, X. Zhao, and X. Shi, "Kinematic behavior analysis of the wadi landslide from time-series sentinel-1 data," *IEEE J. Sel. Topics Appl. Earth Observ. Remote Sens.*, vol. 15, pp. 127–135, Dec. 2022, doi: 10.1109/JS-TARS.2021.3134177.

[11] N. Wang, J. Dong, Z. Wang, J. Lei, L. Zhang, and M. Liao, "Monitoring large-scale hydraulic engineering using Sentinel-1insar: A case study of China's South-to-North water diversion middle route project," *IEEE J. Sel. Topics Appl. Earth Observ. Remote Sens.*, vol. 15, pp. 739–750, Dec. 2022, doi: 10.1109/JSTARS.2021.3138261.

[12] Y. Li et al., "Surface subsidence monitoring and prediction based on PS-InSAR technology and genetic neural network algorithm," *Prog. Geophys.*, vol. 35, no. 3, pp. 845–851, 2020.

[13] Y. He et al., "TS-InSAR analysis for monitoring ground deformation in Lanzhou new district, the loess plateau of China; from 2017–2019," *Adv. Space Res.*, vol. 67, no. 4, pp. 1267–1283, 2021.

[14] M. Simons, "Coseismic deformation from the 1999 mw 7.1 hector mine, California, earthquake as inferred from InSAR and GPS observations," *Bull. Seismol. Soc. Amer.*, vol. 92, no. 4, pp. 1390–1402, 2002.

[15] C. Zhao et al., "Mining collapse monitoring with SAR imagery data: A case study of Datong mine; China," *J. Appl. Remote Sens.*, vol. 8, 2014, Art. no. 83574.

[16] J. Wempen et al., "Comparison of L-band and X-band differential interferometric synthetic aperture radar for mine subsidence monitoring in central Utah," *Int. J. Mining Sci. Technol.*, vol. 27, no. 1, pp. 159–163, 2017.

[17] T. Carlà et al., "Integration of ground-based radar and satellite InSAR data for the analysis of an unexpected slope failure in an open-pit mine," *Eng. Geol.*, vol. 235, pp. 39–52, 2018.

[18] Z. Yang, B. Xu, Z. Li, L. Wu, and J. Zhu, "Prediction of mining-induced Kinematic3D displacements from InSAR using a Weibull model and a Kalman filter," *IEEE Trans. Geosci. Remote Sens.*, vol. 60, 2022, Art. no. 4500912.

[19] J. Li et al., "An application of InSAR time-series analysis for the assessment of mining-induced structural damage in Panji mine, China," *Natural Hazard*, vol. 97, no. 1, pp. 243–258, 2019.

[20] C. Ma et al., "Investigation on mining subsidence based on multi-temporal InSAR and time-series analysis of the small baseline subset—Case study of working faces 22201-1/2 in Bu'ertai mine; Shendong coalfield, China," *Remote Sens.*, vol. 8, 2016, Art. no. 951.

[21] Z. F. Yang, Z. W. Li, J. J. Zhu, J. Hu, Y. J. Wang, and G. L. Chen, "InSAR-based model parameter estimation of probability integral method and its application for predicting mining-induced horizontal and vertical displacements," *IEEE Trans. Geosci. Remote Sens.*, vol. 54, no. 8, pp. 4818–4832, Aug. 2016.

[22] R. Torres et al., "GMES sentinel-1 mission," *Remote Sens. Environ.*, vol. 120, pp. 9–24, 2012.

[23] K. Pawluszek-Filipiak et al., "Integration of DInSAR and SBAS techniques to determine mining-related deformations using sentinel-1 data: The case study of Rydułtowy mine in Poland," *Remote Sens.*, vol. 12, 2020, Art. no. 242.

[24] Y. Tang et al., "Application of grey theory-based model to prediction of land subsidence due to engineering environment in Shanghai," *Environ. Geol.*, vol. 55, no. 3, pp. 583–593, 2008.

[25] J. Bao et al., "Application of gray model in prediction of mining area subsidence," *Ind. Mine Automat.*, vol. 38, no. 5, pp. 46–49, 2012.

[26] S. Ye et al., "Three-dimensional numerical modeling of land subsidence in Shanghai, China," *Hydrogeol. J.*, vol. 24, no. 3, pp. 695–709, 2016.

[27] Y. Chen et al., "Prediction of InSAR deformation time-series using a long short-term memory neural network," *Int. J. Remote Sens.*, vol. 42, no. 18, pp. 6921–6944, 2021.

[28] T. Zhang et al., *Prediction Modeling and Analysis of Urban Land Subsidence Based on SBAS-InSAR*. Beijing, China: Beijing Univ. Civil Eng. Architecture, 2020.

[29] G. Dong, *Study on Forecasting Model of Land Subsidence and Its Application*. Tianjin, China: Tianjin Univ., 2006.

[30] Y. He et al., "A unified network of information considering superimposed landslide factors sequence and pixel spatial neighbourhood for landslide susceptibility mapping," *Int. J. Appl. Earth Observ. Geoinf.*, vol. 104, 2021, Art. no. 102508.

[31] P. Li et al., "Time series prediction of mining subsidence based on a SVM," *Mining Sci. Technol.*, vol. 21, no. 4, pp. 557–562, 2011.

[32] Q. Liu, Y. Zhang, J. Wei, H. Wu, and M. Deng, "HLSTM: Heterogeneous long short-term memory network for large-scale InSAR ground subsidence prediction," *IEEE J. Sel. Topics Appl. Earth Observ. Remote Sens.*, vol. 14, pp. 8679–8688, Aug. 2021, doi: 10.1109/JSTARS.2021.3106666.

[33] H. Sak et al., "Long short-term memory recurrent neural network architectures for large scale acoustic modeling," *Comput. Sci.*, 2014.

[34] F. Ma et al., "Ground movement resulting from underground backfill mining in a nickel mine (Gansu Province; China)," *Natural Hazard.*, vol. 77, no. 3, pp. 1475–1490, 2015.

[35] X. Geng et al., *Deformation Monitoring Based on InSAR in Longshou Mining Area*. Qingdao, China: Shandong Univ. Sci. Technol., 2018.

[36] Q. Li, *Surface Subsidence Monitoring of Jinchuan Mining Area Based on Space-Earth Data Integration*. Mianyang, China: Southwest Univ. Sci. Technol., 2020.

[37] N. Ding et al., "Study on three-dimensional deformation law of longshou open-pit based on InSAR and GPS," *Metal Mine*, vol. 10, pp. 61–67, 2019.

[38] Q. Sun et al., "Deformation failure mechanism of deep vertical shaft in Jinchuan mining area," *Sustainability*, vol. 12, no. 6, pp. 2226–2248, 2020.

[39] Y. Zhang et al., "Numerical analysis and monitoring of local instability characteristics of open-pit slope," *Metal Mine*, vol. 10, pp. 142–147, 2014.

[40] P. Berardino, G. Fornaro, R. Lanari, and E. Sansosti, "A new algorithm for surface deformation monitoring based on small baseline differential SAR interferograms," *IEEE Trans. Geosci. Remote Sens.*, vol. 40, no. 11, pp. 2375–2383, Nov. 2002.

[41] Y. Wang et al., "Comparative study of landslide susceptibility mapping with different recurrent neural networks," *Comput. Geosci.*, vol. 138, 2020, Art. no. 104445.

[42] K. Cho et al., "Learning phrase representations using RNN encoder-decoder for statistical machine translation," 2014, *arXiv:1406.1078*.

[43] S. Hochreiter et al., "Long short-term memory," *Neural Comput.*, vol. 9, no. 8, pp. 1735–1780, 1997.

[44] F. Gers et al., "Learning precise timing with LSTM recurrent networks," *J. Mach. Learn Res.*, vol. 3, no. 1, pp. 115–143, 2003.

[45] D. Kingma et al., "Adam: A method for stochastic optimization," 2015, *arXiv:1412.6980*.

[46] Q. Deng et al., "Uplift mechanism of the bottom of open pit after the transition from open-pit mining to underground mining in Longshou mine," *J. Mining Saf. Eng.*, vol. 32, no. 4, pp. 677–682, 2015.

[47] B. Peck et al., "Deep excavations and tunneling in soft ground," in *Proc. 7th Int. Conf. Soil Mech. Found. Eng.*, 1969, pp. 225–290.

[48] X. Liu et al., "Three-dimensional and long-term landslide displacement estimation by fusing C- and L-band SAR observations: A case study in Gongjue county; Tibet; China," *Remote Sens. Environ.*, vol. 267, 2021, Art. no. 112745.

[49] Y. Aimaiti et al., "Multi-sensor InSAR analysis of progressive land subsidence over the coastal city of Urayasu, Japan," *Remote Sens.*, vol. 10, 2018, Art. no. 1304.

[50] W. Yang et al., "InSAR monitoring of 3D surface deformation in Jinchuan mining area; Gansu province," *Remote Sens. Natural Resour.*, vol. 34, no. 1, pp. 177–188, 2022.

[51] Y. He et al., "Characteristics of surface deformation in Lanzhou with Sentinel-1A TOPS," *Geosciences*, vol. 10, 2020, Art. no. 99.

[52] Z. Liu et al., "Surface deformation monitoring based on SBAS-InSAR in Changzhi mining area," *Remote Sens. Land Resour.*, vol. 26, no. 3, pp. 37–42, 2014.

[53] H. Prichard et al., "Distribution of platinum-group elements in magmatic and altered ores in the Jinchuan intrusion; China: An example of selenium remobilization by postmagmatic fluids," *Mineralium Deposita*, vol. 48, no. 6, pp. 767–786, 2013.

[54] X. Li et al., "Ground surface movement and fissures induced by underground mining in the Jinchuan nickel mine," *Eng. Geol.*, vol. 76, no. 2, pp. 93–107, 2004.

[55] F. Ma et al., "Vertical shaft collapse at the Jinchuan nickel mine, Gansu Province, China: Analysis of contributing factors and causal mechanisms," *Environ. Earth Sci.*, vol. 69, no. 1, pp. 21–28, 2013.

[56] C. Juang et al., "Loess geohazards research in China: Advances and challenges for mega engineering projects," *Eng. Geol.*, vol. 251, pp. 1–10, 2019.

[57] Z. Yuan et al., "Collapsibility and seismic settlement of loess," *Eng. Geol.*, vol. 105, pp. 119–123, 2009.

[58] Q. Wu et al., "SBAS-InSAR based deformation detection of urban land, created from mega-scale mountain excavating and valley filling in the loess plateau: The case study of Yan'an City," *Remote Sens.*, vol. 11, 2019, Art. no. 1673.

[59] F. A. Gers and J. Schmidhuber, "Recurrent nets that time and count," in *Proc. IEEE-INNS-ENNS Int. Joint Conf. Neural Netw. Neural Comput.: New Challenges Perspectives New Millennium*, 2000, pp. 189–194.

Haowen Yan received the Ph.D. degree in cartography and geographical information engineering from the Wuhan University, Wuhan, China, in 2002, and the Ph.D. degree in geography and environmental management from the Waterloo University, Waterloo, ON, Canada, in 2014.

He is currently an Editor-in-Chief of *Journal of Geo-visualization and Spatial Analysis*. He is the Dean of the Faculty of Geomatics, Lanzhou Jiaotong University, Lanzhou, China, and the Director of the National-Local Joint Engineering Research Center of Technologies and Applications for National Geographic State Monitoring, Lanzhou, China. His research interests include WeMaps, automated map generalization, spatial relations, geovisualization and spatial analysis, spatial data finger-printing and watermarking, history of maps, and cartography.
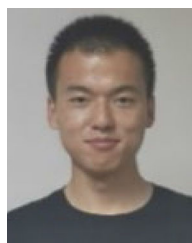
Wang Yang received the B.E. degree in remote sensing science and technology from the Lanzhou Jiaotong University, Lanzhou, China, in 2019. He is currently working toward the M.S. degree in surveying and mapping with the Faculty of Geomatics, Lanzhou Jiaotong University, Lanzhou, China.

His research interests include InSAR data processing technology, machine learning, and remote sensing image information extraction.

Sheng Yao received the B.E. degree in digital media technology from the North China University of Technology, Beijing, China, in 2020. He is currently working toward the M.S. degree in surveying and mapping with the Faculty of Geomatics, Lanzhou Jiaotong University, Lanzhou, China.

His research interests include application of remote sensing in deep learning.

Lifeng Zhang received the M.S. degree in cartography and geographic information system from the Lanzhou Jiaotong University, Lanzhou, China, in 2010, and the Ph.D. degree in environmental science and engineering from the Lanzhou Jiaotong University, Lanzhou, China, in 2017.

He is currently an Associate Professor with the Lanzhou Jiaotong University, Lanzhou, China. His research interests include ecological environment remote sensing monitoring, visualized analysis, and analysis of land use change.

Yi Chen received the B.E. degree in remote sensing science and technology from the Lanzhou Jiaotong University, Lanzhou, China, in 2018, and the M.S. degree in surveying and mapping from the Lanzhou Jiaotong University, Lanzhou, China, in 2022.

His research interests include land subsidence monitoring and prediction, and deep learning.

Yi He received the B.S. degree in geographic information system from the Lanzhou Jiaotong University, Lanzhou, China, in 2011, and the Ph.D. degree in earth system science from the Lanzhou University, Lanzhou, China, in 2016.

He is currently a Postdoctoral Researcher with the School of Environment and Municipal Engineering, Lanzhou Jiaotong University, Lanzhou, China. He is also an Associate Professor with the faculty of geomatics, Lanzhou Jiaotong University, Lanzhou, China. His research interests include disaster remote sensing, ecological remote sensing, image processing, and time-series InSAR prediction based on deep learning.

Tao Liu received the Ph.D. degree in cartography and geographical information engineering from the Wuhan University, Wuhan, China, in 2011.

He is currently a Professor with the Faculty of Geomatics, Lanzhou Jiaotong University, Lanzhou, China. His research interests include spatial relation theory, GIS and RS integration, and application and development of GIS and RS.

Prof. Liu is a member of the theory and method work committee of China Geographic Information Industry Association.